mathematics

MDPI

Article

Phase-Variation Operators, Essential Spectrum, and Galerkin Bounds for Fixed-Region Fourier Energy

Yinlong Hou *, Haonan Jin, Ni Zhang, Ruixia Liu and Liyin Zhang

School of Artificial Intelligence, School of Automation, Xi'an University of Posts and Telecommunications, Xi'an 710121, China; 19173140602@stu.xupt.edu.cn (H.J.); zhangni@xupt.edu.cn (N.Z.); ruixialiu@xupt.edu.cn (R.L.); zhangliyin@xupt.edu.cn (L.Z.)
* Correspondence: houyinlong@xupt.edu.cn

Abstract

We study how aperture phase changes Fourier energy within a fixed receiving region. For uniform amplitude and a finite centrally symmetric receiver, a bounded self-adjoint operator represents the quadratic variation. Its compact-minus-multiplication structure gives an exact characterization of the essential spectral interval on the radial disk space. The lower spectral endpoint is unattained at every positive receiver radius, while nested Galerkin spaces recover both endpoints. Rational certificates establish isolated upper eigenvalues at radii 11/10 and 2, and operator-norm continuity extends this separation to explicit intervals. A mean-zero L^4 identity gives uniform quartic remainder bounds, with finite-dimensional coefficients obtained from an exact polynomial embedding constant. On real L^2, the energy has a globally Lipschitz first Fréchet derivative and a bounded second Gâteaux derivative at zero in the dual norm. At every positive disk-receiver radius, concentrating phases preclude a second-order Fréchet Taylor expansion at zero on the radial and full two-dimensional piston-free disk spaces. The resulting distinction between controlled phase classes and the full RMS sphere determines where spectral bounds yield uniform nonlinear approximations.

Keywords: fourier concentration; phase variation; self-adjoint operator; essential spectrum; Galerkin approximation; quartic remainder; radial phase

MSC: 47A10

1. Introduction

The Fourier energy received within a fixed region depends nonlinearly on the aperture phase. With aperture amplitude fixed, a root-mean-square (RMS) phase constraint leaves the spatial distribution of phase unrestricted. We examine the extremal quadratic responses and the conditions under which they approximate the nonlinear energy uniformly. Enlarging a finite modal space changes both questions: spectral endpoints can become unattained, and fixed-direction expansions can lose uniformity over the RMS sphere.

Fourier concentration has a classical integral-operator formulation [1,2]. Clements and Wilkins [3] used Fredholm eigenvalue and Rayleigh–Ritz methods for encircled-energy optimization; optical eigenmodes similarly optimize quadratic field observables [4]. Phase-only point-spread-function expansions already retain both second-order field contributions [5,6]. Antonello et al. [7] derive a semidefinite quadratic imaging metric after neglecting the finite pinhole size. We retain the fixed-region integral. A motivating setting is wavefront testing of high-power optical components with finite focal-plane apertures, where phase errors alter the energy collected within a fixed region.

Check for updates

Academic Editor: Luigi Rodino

Received: 8 October 2026
Revised: 28 October 2026
Accepted: 29 October 2026
Published: 8 November 2026

Copyright: © 2026 by the authors. Licensee MDPI, Basel, Switzerland. This article is an open access article distributed under the terms and conditions of the Creative Commons Attribution (CC BY) license.

Parameterized surface-error studies motivate the dependence on phase shape. Aryan et al. [8,9] relate anisotropic mid-spatial frequency errors to directional modulation, including the minimum modulation curve. Hefferan et al. [10] fix the encircled or ensquared energy at 90% and analyze the corresponding radius or extent as tooling-mark parameters vary. Liu et al. [11] study optical tolerance analysis for radial single-frequency errors. Here, we keep the receiver fixed and analyze a dimensionless energy functional on phase space. System-specific tolerance allocation is outside this model.

Pupil-difference probability-distribution (PDPD) moments provide a close connection. DeMars and Suleski [12,13] use difference moments to predict modulation changes, and DeMars et al. [14] incorporate them into an optical modeling workflow. Equation (16) expresses the present quadratic coefficient as a receiver-weighted second difference moment. For radial phases, the overlap mean vanishes, so the raw and central second moments coincide. We use this fixed-receiver functional to identify a bounded self-adjoint phase-variation operator and study its spectrum and topology-dependent remainder.

The closest operator-theoretic precedents concern multiplication operators and their compact perturbations. Biberdorf and Väth [15] determine essential spectra for compact perturbations of orthomorphisms on non-atomic function spaces. Morrison [16] studies finite spectral approximations of multiplication operators, including Legendre bases. Finite Hankel theory describes the compact concentration component in circular geometry [17]. Weyl and Rayleigh–Ritz theory [18] supplies the essential-spectrum and Galerkin principles used below.

For uniform aperture amplitude, the second-order baseline-field contribution produces the multiplication term in $T_\Omega = K_\Omega - M_{b_\Omega}$. For radial phases on a disk with uniform aperture amplitude and a centered disk receiver, strict positivity of K_Ω determines the lower spectral endpoint and excludes a unit phase attaining it. Rational certificates and continuity establish upper spectral separation on two radius intervals. The exact essential-spectrum interval and these endpoint results are established for this model; no extension to general apertures or nonuniform amplitudes is claimed. An exact polynomial embedding constant then converts the L^4 remainder estimate into uniform bounds on finite modal spheres.

The nonlinear approximation has a different scope on the full RMS sphere. Although the first derivative is globally Lipschitz and directionally differentiable in the dual norm, concentration prevents a second-order Fréchet Taylor expansion at zero. An exact concentrating-phase identity establishes this failure for every positive disk-receiver radius. This nonlocal example connects the phase-variation problem with regularity limitations caused by concentration in Lebesgue spaces [19].

2. Fixed-Region Fourier-Energy Functional

The difference-kernel representation and cosine expansion below give the standard phase-variation formulas used in the operator analysis. Let $D \subset \mathbb{R}^2$ be bounded and measurable, with positive area. Let $A \in L^2(D)$ be real and nonnegative, and set

$$S = \int_D A(\boldsymbol{r})^2 \, \mathrm{d}\boldsymbol{r} > 0. \tag{1}$$

All aperture fields are extended by zero outside D. Our Fourier convention is

$$\hat{f}(\boldsymbol{q}) = \int_D f(\boldsymbol{r}) e^{-2\pi \mathrm{i} \boldsymbol{q}\cdot\boldsymbol{r}} \, \mathrm{d}\boldsymbol{r}. \tag{2}$$

Finite area implies $A \in L^1(D)$. For a real measurable phase ϕ, finite almost everywhere, the field $Ae^{\mathrm{i}\phi}$ belongs to $L^1 \cap L^2$.

Definition 1 (Fixed-region energy)**.** *Let $\Omega \subset \mathbb{R}^2$ be measurable, of finite area, and independent of the phase. Define*

$$E_\Omega(\phi) = \frac{1}{S}\int_\Omega |\widehat{Ae^{i\phi}}(\boldsymbol{q})|^2 \,\mathrm{d}\boldsymbol{q}, \qquad \kappa_\Omega(\boldsymbol{x}) = \int_\Omega e^{-2\pi i \boldsymbol{q}\cdot\boldsymbol{x}}\,\mathrm{d}\boldsymbol{q}. \tag{3}$$

Plancherel's identity gives $0 \le E_\Omega(\phi) \le 1$. The denominator is the total aperture energy, without renormalization to a finite frequency window. Adding a constant phase does not change E_Ω.

Theorem 1 (Real difference kernel)**.** *Suppose $\Omega = -\Omega$ up to null sets. Then, κ_Ω is real, continuous, even, and bounded in modulus by $|\Omega|$. Moreover,*

$$E_\Omega(\phi) = \frac{1}{S}\iint_{D\times D} A(\boldsymbol{r})A(\boldsymbol{s})\kappa_\Omega(\boldsymbol{r}-\boldsymbol{s})\cos\big(\phi(\boldsymbol{r})-\phi(\boldsymbol{s})\big)\,\mathrm{d}\boldsymbol{r}\,\mathrm{d}\boldsymbol{s}. \tag{4}$$

In particular, $E_\Omega(\epsilon\psi) = E_\Omega(-\epsilon\psi)$.

Proof. Continuity and the bound follow by dominated convergence in (3). Inversion symmetry cancels the imaginary part and gives evenness of the kernel. Expanding the squared Fourier integral is justified by the absolute bound $|\Omega|\|A\|_1^2$ on the integral over $\Omega \times D \times D$. After integration over Ω, exchanging $\boldsymbol{r}$ and $\boldsymbol{s}$ cancels the sine term. This proves (4); its cosine is even in ϵ. □

Central symmetry is required only of the fixed receiver, modulo null sets. The aperture and phase may be nonradial. The evenness concerns integrated energy about the zero-phase baseline; pointwise intensity need not share this symmetry.

3. Second-Order Phase Variation and Quartic Control

For bounded real ψ, define $\Delta\psi = \psi(\boldsymbol{r}) - \psi(\boldsymbol{s})$.

Theorem 2 (Quadratic coefficient and absolute remainder)**.** *Under the assumptions of Theorem 1, if $\psi \in L^\infty(D)$, then for every real ϵ,*

$$E_\Omega(\epsilon\psi) = E_\Omega(0) + \epsilon^2 Q_\Omega[\psi] + R_4, \tag{5}$$

$$Q_\Omega[\psi] = -\frac{1}{2S}\iint_{D\times D} AA'\kappa_\Omega(\boldsymbol{r}-\boldsymbol{s})(\Delta\psi)^2\,\mathrm{d}\boldsymbol{r}\,\mathrm{d}\boldsymbol{s}, \tag{6}$$

$$\begin{aligned} |R_4| &\le \frac{|\epsilon|^4}{24S}\iint_{D\times D} |AA'\kappa_\Omega(\boldsymbol{r}-\boldsymbol{s})|\,|\Delta\psi|^4\,\mathrm{d}\boldsymbol{r}\,\mathrm{d}\boldsymbol{s} \\ &\le \frac{2|\epsilon|^4}{3S}|\Omega|\|A\|_1^2\|\psi\|_\infty^4. \end{aligned} \tag{7}$$

Here, $AA' = A(\boldsymbol{r})A(\boldsymbol{s})$. The equivalent frequency expression is

$$Q_\Omega[\psi] = \frac{1}{S}\int_\Omega \Big\{|\widehat{A\psi}|^2 - \mathrm{Re}\Big(\overline{\widehat{A}}\,\widehat{A\psi^2}\Big)\Big\}\,\mathrm{d}\boldsymbol{q}. \tag{8}$$

Proof. For real t, the Taylor remainder satisfies $|\cos t - 1 + t^2/2| \le |t|^4/24$. Insert $t = \epsilon\Delta\psi$ into (4). All resulting integrals are finite. The last bound uses $|\Delta\psi| \le 2\|\psi\|_\infty$ and $|\kappa_\Omega| \le |\Omega|$. Expanding $(\Delta\psi)^2$, the mixed product gives the first term of (8); the two squared terms give its real cross term. Fubini is again justified by $A \in L^1$ and bounded ψ. □

Thus, $\frac{\mathrm{d}^2}{\mathrm{d}\epsilon^2}E_\Omega(\epsilon\psi)|_{\epsilon=0} = 2Q_\Omega[\psi]$. The cross term in (8) distinguishes phase variation from the nonnegative field-concentration term.

Polarization defines the real symmetric form

$$\mathcal{B}_\Omega(f,g) = -\frac{1}{2S}\iint_{D\times D} AA'\kappa_\Omega(\boldsymbol{r}-\boldsymbol{s})(f(\boldsymbol{r})-f(\boldsymbol{s}))(g(\boldsymbol{r})-g(\boldsymbol{s}))\,\mathrm{d}\boldsymbol{r}\,\mathrm{d}\boldsymbol{s}. \tag{9}$$

For general $A \in L^2$, the statements so far apply to bounded phase directions. Extending this form to a specified RMS Hilbert space requires a further argument.

4. Phase-Variation Operator

For this section, take $A = 1$ on D, so $S = |D|$. Define the probability area measure and real Hilbert spaces

$$\mathrm{d}\mu(\boldsymbol{r}) = \frac{\mathrm{d}\boldsymbol{r}}{S}, \qquad \mathcal{H} = L^2(D,\mu;\mathbb{R}), \qquad \mathcal{H}_0 = \{f \in \mathcal{H} : \langle f,1\rangle_\mu = 0\}. \tag{10}$$

For $1 \le p < \infty$, $\|f\|_p = (\int_D |f|^p\,\mathrm{d}\mu)^{1/p}$; $\|f\|_\infty$ is the essential supremum. Unsubscripted Hilbert norms mean $\|f\|_2$. The inner product is $\langle f,g\rangle_\mu = \int_D fg\,\mathrm{d}\mu$; its induced norm is the area RMS. Spectra below refer to the complexification of the real self-adjoint operator. Real and complex Rayleigh endpoints coincide.

For nonuniform A, an intensity-RMS space would instead use $A^2\,\mathrm{d}\boldsymbol{r}/S$. The corresponding multiplier contains $(K_\Omega A)/A$ on $\{A > 0\}$, which need not be bounded under $A \in L^2$ alone. All operator results below therefore use uniform amplitude and the area-RMS norm in (10).

Theorem 3 (Bounded self-adjoint phase variation)**.** *Let Ω have finite area and satisfy $\Omega = -\Omega$ modulo null sets. Set*

$$(K_\Omega f)(\boldsymbol{r}) = \int_D \kappa_\Omega(\boldsymbol{r}-\boldsymbol{s})f(\boldsymbol{s})\,\mathrm{d}\boldsymbol{s}, \quad b_\Omega = K_\Omega 1, \quad T_\Omega = K_\Omega - M_{b_\Omega}, \tag{11}$$

where $M_b f = bf$. Then, K_Ω is a positive self-adjoint Hilbert–Schmidt contraction, and b_Ω is real, continuous and bounded. The form (9) extends uniquely to a bounded symmetric form on $\mathcal{H}$, represented by T_Ω:

$$\mathcal{B}_\Omega(f,g) = \langle T_\Omega f,g\rangle_\mu, \qquad \|T_\Omega\| \le L_\Omega := \min\{S|\Omega|,\, 1 + \|b_\Omega\|_\infty\}. \tag{12}$$

Furthermore, $T_\Omega 1 = 0$, and $\mathcal{H}_0$ reduces T_Ω.

Proof. Relative to μ, the integral kernel of K_Ω is $S\kappa_\Omega$, a bounded function on a finite measure product space. It is therefore Hilbert–Schmidt. Its real symmetric kernel gives self-adjointness. Fubini and Plancherel give

$$\langle K_\Omega f,f\rangle_\mu = \frac{1}{S}\int_\Omega |\hat{f}|^2\,\mathrm{d}\boldsymbol{q}, \qquad 0 \le \langle K_\Omega f,f\rangle_\mu \le \|f\|_\mu^2. \tag{13}$$

Additionally, $|b_\Omega| \le S|\Omega|$; continuity follows by dominated convergence. Hence, both operators in (11) are bounded and self-adjoint.

To obtain the direct bound for the form, observe that

$$\iint |f(\boldsymbol{r})-f(\boldsymbol{s})|^2\,\mathrm{d}\mu(\boldsymbol{r})\,\mathrm{d}\mu(\boldsymbol{s}) = 2\big(\|f\|_\mu^2 - |\langle f,1\rangle_\mu|^2\big). \tag{14}$$

Put $c = \|\kappa_\Omega\|_\infty \le |\Omega|$ and $\Delta f = f(\boldsymbol{r}) - f(\boldsymbol{s})$. For arbitrary $f,g \in \mathcal{H}$, Cauchy–Schwarz and (14) imply

$$\frac{S}{2}\iint |\kappa_\Omega \Delta f \Delta g|\,\mathrm{d}\mu\,\mathrm{d}\mu \le \frac{Sc}{2}\|\Delta f\|_{L^2(\mu\times\mu)}\|\Delta g\|_{L^2(\mu\times\mu)} \le Sc\|f\|_2\|g\|_2. \tag{15}$$

Thus, the integral in (9), after conversion to a probability measure, is absolutely convergent for all $f, g \in \mathcal{H}$ and defines a bounded symmetric form there. To make the extension explicit, take bounded truncations $f_n \to f$ and $g_n \to g$ in L^2. Then,

$$|\mathcal{B}_\Omega(f_n, g_n) - \mathcal{B}_\Omega(f, g)| \le Sc\{\|f_n - f\|_2 \|g_n\|_2 + \|f\|_2 \|g_n - g\|_2\} \longrightarrow 0.$$

The same estimate proves independence of the approximating sequences and uniqueness of the continuous extension. Subtracting the means also gives bounded approximants in $\mathcal{H}_0$ when required.

For each f, the Riesz representation theorem gives a unique vector $\widetilde{T}f$ with $\mathcal{B}_\Omega(f, g) = \langle \widetilde{T}f, g \rangle_\mu$ for all g, and $\|\widetilde{T}f\|_2 \le Sc\|f\|_2$. Bilinearity and symmetry make $\widetilde{T}$ linear and self-adjoint. Expanding the phase differences and using the real symmetric kernel yields $\widetilde{T} = K_\Omega - M_{b_\Omega}$ on bounded functions. Boundedness and density extend this identity to $\mathcal{H}$. This proves the direct norm bound in (12); the decomposition and $\|K_\Omega\| \le 1$ give the other bound. Finally, $K_\Omega 1 = b_\Omega$ implies $T_\Omega 1 = 0$, and self-adjointness gives $\langle T_\Omega f, 1 \rangle_\mu = 0$ for $f \in \mathcal{H}_0$. □

Riesz representation uses boundedness of the form; coercivity is not needed. The identity $T_\Omega 1 = 0$ excludes positive coercivity on $\mathcal{H}$, and the form need not be positive on $\mathcal{H}_0$. For $f \in \mathcal{H}$, define $Q_\Omega[f] = \mathcal{B}_\Omega(f, f)$ by this continuous extension. The compactness of K_Ω does not imply the compactness of T_Ω. The multiplication term will determine an essential spectral interval in the radial model.

4.1. Relation to Pupil-Difference Moments

For bounded real f, put $D_{\boldsymbol{\tau}} = D \cap (D + \boldsymbol{\tau})$ and $C_D(\boldsymbol{\tau}) = |D_{\boldsymbol{\tau}}|$. When $C_D(\boldsymbol{\tau}) > 0$, let $m_1(\boldsymbol{\tau})$ and $v_2(\boldsymbol{\tau})$ be the mean and variance, under a uniform measure on $D_{\boldsymbol{\tau}}$, of $f(\boldsymbol{r}) - f(\boldsymbol{r} - \boldsymbol{\tau})$. Define the products with C_D to be zero when the overlap has zero area. Changing variables $\boldsymbol{\tau} = \boldsymbol{r} - \boldsymbol{s}$ in (6) gives

$$Q_\Omega[f] = -\frac{1}{2S} \int_{\mathbb{R}^2} \kappa_\Omega(\boldsymbol{\tau}) C_D(\boldsymbol{\tau}) [v_2(\boldsymbol{\tau}) + m_1(\boldsymbol{\tau})^2] \, \mathrm{d}\boldsymbol{\tau}. \tag{16}$$

The same absolute bound used in Theorem 2 justifies this change of variables. The difference variable matches the construction in DeMars et al. [14] (Equations (12) and (13)); their moments are centered on the overlap. If $D = -D$ modulo null sets and $f(-\boldsymbol{r}) = f(\boldsymbol{r})$, the map $\boldsymbol{r} \mapsto \boldsymbol{\tau} - \boldsymbol{r}$ preserves $D_{\boldsymbol{\tau}}$ and reverses the difference. Hence, $m_1(\boldsymbol{\tau}) = 0$, including for every radial phase on the disk. In this case, the second moment in (16) is precisely the central second difference moment. This receiver-weighted functional is the starting point for the spectral and regularity analysis below.

4.2. Quartic Control on Mean-Zero L^4 Classes

For uniform aperture amplitude, write $S = |D|$, $\mathrm{d}\mu = \mathrm{d}\boldsymbol{r}/S$, and $\Delta f = f(\boldsymbol{r}) - f(\boldsymbol{s})$. All norms in this subsection use the probability measure μ. The receiver has finite measure and is centrally symmetric, so its difference kernel κ_Ω is real and even.

Theorem 4 (L^4 quartic control). *For every real, mean-zero $f \in L^4(D, \mu)$,*

$$\iint_{D \times D} |\Delta f|^4 \, \mathrm{d}\mu \, \mathrm{d}\mu = 2\|f\|_4^4 + 6\|f\|_2^4. \tag{17}$$

For every real ϵ,

$$\left| E_\Omega(\epsilon f) - E_\Omega(0) - \epsilon^2 Q_\Omega[f] \right| \le \frac{S|\Omega|}{12} \left(\|f\|_4^4 + 3\|f\|_2^4 \right) |\epsilon|^4. \tag{18}$$

On the uniform unit disk with a centered receiver of radius q_0, this becomes

$$\left|E_{q_0}(\epsilon f) - E_{q_0}(0) - \epsilon^2 Q_{q_0}[f]\right| \le \frac{\pi^2 q_0^2}{12}\left(\|f\|_4^4 + 3\|f\|_2^4\right)|\epsilon|^4. \tag{19}$$

The disk estimate applies in particular to radial phases with $\mathrm{d}\mu(\rho) = 2\rho\,\mathrm{d}\rho$.

Proof. Since μ is a probability measure, all moments of f through order four are integrable. Expanding the fourth power and applying Fubini gives $2m_4 - 8m_1m_3 + 6m_2^2$, where $m_j = \int f^j\,\mathrm{d}\mu$. The zero mean proves (17). In the exact cosine-kernel formula, the change from area to probability measure gives $E_\Omega(h) = S\iint \kappa_\Omega \cos(\Delta h)\,\mathrm{d}\mu\,\mathrm{d}\mu$. The inequality $|\cos t - 1 + t^2/2| \le |t|^4/24$ therefore bounds the remainder by $S|\Omega||\epsilon|^4\iint |\Delta f|^4\,\mathrm{d}\mu\,\mathrm{d}\mu/24$. Substitution of (17) proves (18). For the two disks, $S = \pi$ and $|\Omega| = \pi q_0^2$, proving (19). No pointwise bound on f was used. □

On a mean-zero unit L^2 sphere, a common bound on $\|f\|_4$ gives uniform quartic control. A common bound $\|f\|_\infty \le M$ suffices because $\|f\|_4^4 \le M^2\|f\|_2^2 = M^2$.

4.3. Differentiability at Zero in the RMS Topology

Here, $\mathcal{H} = L^2(D,\mu;\mathbb{R})$ and $\mathcal{H}_0 = 1^\perp$, with uniform aperture and a finite centrally symmetric receiver. We use the norm Gâteaux derivative of the first derivative map $DE_\Omega : \mathcal{H} \to \mathcal{H}^*$. At a point h, this means that there is a bounded linear map $A_h : \mathcal{H} \to \mathcal{H}^*$ such that

$$\left\|\frac{DE_\Omega(h+tf) - DE_\Omega(h)}{t} - A_h f\right\|_{\mathcal{H}^*} \longrightarrow 0 \qquad \text{for every fixed } f \in \mathcal{H}.$$

The dual norm makes convergence uniform over $\|g\|_2 \le 1$, which is stronger than testing against each fixed g. The perturbation direction f remains fixed. Uniformity over unit directions f would be required for Fréchet differentiability of DE_Ω.

Proposition 1 (First Fréchet and second Gâteaux derivatives)**.** *The functional E_Ω is continuously Fréchet differentiable on $\mathcal{H}$ with a globally Lipschitz derivative. At zero,*

$$DE_\Omega(0) = 0, \qquad D^2_G E_\Omega(0)[f,g] = 2\langle T_\Omega f, g\rangle_\mu. \tag{20}$$

The second derivative is understood precisely as

$$\lim_{t\to 0}\left\|\frac{DE_\Omega(tf) - DE_\Omega(0)}{t} - 2\langle T_\Omega f, \cdot\rangle_\mu\right\|_{\mathcal{H}^*} = 0 \quad \textit{for each fixed } f \in \mathcal{H}. \tag{21}$$

Every fixed direction satisfies $E_\Omega(\epsilon f) = E_\Omega(0) + \epsilon^2 Q_\Omega[f] + o(\epsilon^2)$. The assertions also hold on $\mathcal{H}_0$ by restriction. On a finite-dimensional space of bounded phases, the ordinary coefficient Hessian at zero is twice the Galerkin matrix of T_Ω.

Proof. Write $c = \|\kappa_\Omega\|_\infty \le |\Omega|$. For $h, g \in \mathcal{H}$ set

$$DE_\Omega(h)[g] = -S\iint \kappa_\Omega \sin(\Delta h)\Delta g\;\mathrm{d}\mu\,\mathrm{d}\mu. \tag{22}$$

This is bounded and linear in g. The pointwise cosine Taylor inequality gives

$$|E_\Omega(h+g) - E_\Omega(h) - DE_\Omega(h)[g]| \le \frac{Sc}{2}\iint (\Delta g)^2\,\mathrm{d}\mu\,\mathrm{d}\mu \le Sc\|g\|_2^2,$$

which proves Fréchet differentiability. The Lipschitz property of sine and Cauchy–Schwarz give $\|DE_\Omega(h_1) - DE_\Omega(h_2)\|_{\mathcal{H}^*} \le 2Sc\|h_1 - h_2\|_2$. Equation (22) gives $DE_\Omega(0) = 0$.

For fixed $h, f \in \mathcal{H}$ and $t \neq 0$, let

$$a_t = \frac{\sin(\Delta h + t\Delta f) - \sin(\Delta h)}{t} - \cos(\Delta h)\Delta f$$
$$= \Delta f \int_0^1 \{\cos(\Delta h + \theta t \Delta f) - \cos(\Delta h)\}\, \mathrm{d}\theta.$$

Both phase differences are finite almost everywhere, so $a_t \to 0$ almost everywhere. Moreover,

$$|a_t|^2 \le 4|\Delta f|^2, \qquad \iint 4|\Delta f|^2 \,\mathrm{d}\mu \,\mathrm{d}\mu \le 8\|f\|_2^2 < \infty.$$

Dominated convergence applied to $|a_t|^2$ gives $\|a_t\|_{L^2(\mu\times\mu)} \to 0$, without any L^4 or pointwise bound on f. The symmetric bilinear form $B_h(f,g) = -S \iint \kappa_\Omega \cos(\Delta h)\Delta f \Delta g \,\mathrm{d}\mu \,\mathrm{d}\mu$ obeys $|B_h(f,g)| \le 2Sc\|f\|_2\|g\|_2$. Thus, $A_h f = B_h(f,\cdot)$ defines a bounded linear map from $\mathcal{H}$ to $\mathcal{H}^*$. Taking the supremum over $\|g\|_2 \le 1$ and using (14) gives

$$\left\| \frac{DE_\Omega(h+tf) - DE_\Omega(h)}{t} - B_h(f,\cdot) \right\|_{\mathcal{H}^*} \le \sqrt{2}Sc\|a_t\|_{L^2(\mu\times\mu)} \longrightarrow 0.$$

At $h = 0$, expansion of the phase differences gives $B_0(f,g) = 2\langle T_\Omega f, g\rangle_\mu$, proving (21). For a fixed f, dominated convergence with $|\cos(\epsilon\Delta f) - 1|/\epsilon^2 \le |\Delta f|^2/2$ proves the directional expansion. Bounded finite mode functions justify ordinary coefficient differentiation, giving the last assertion. □

For the disk model with positive receiver radius, Section 8 constructs concentrating directions for which $E_\Omega(h) - E_\Omega(0) - Q_\Omega[h]$ is not $o(\|h\|_2^2)$. Thus, the fixed-direction result does not yield a second-order Fréchet Taylor expansion at zero in this model.

5. RMS-Constrained Spectral Bounds and Galerkin Approximation

Write $T_0 = T_\Omega|_{\mathcal{H}_0}$. For a unit phase, the quadratic response lies between

$$\alpha = \inf_{\substack{f\in\mathcal{H}_0 \\ \|f\|=1}} \langle T_0 f, f\rangle = \inf \sigma(T_0), \qquad \beta = \sup_{\substack{f\in\mathcal{H}_0 \\ \|f\|=1}} \langle T_0 f, f\rangle = \sup \sigma(T_0). \tag{23}$$

The spectral equalities follow from the Rayleigh characterization for bounded self-adjoint operators [18] (Theorem 2.20); attainment requires a corresponding eigenvector. For each fixed unit f, Proposition 1 gives $E_\Omega(\epsilon f) - E_\Omega(0) = \epsilon^2 Q_\Omega[f] + o(\epsilon^2)$. Hence, α and β bound the quadratic change in the fraction of total energy captured by the receiver. A negative coefficient describes a loss within the receiver, and a positive one describes a gain, with total Fourier energy conserved. If changes are normalized by $E_\Omega(0) > 0$, the bounds become $\alpha/E_\Omega(0)$ and $\beta/E_\Omega(0)$. Uniform finite-amplitude estimates follow under the phase-class bounds in Theorem 4.

Let $(e_j)_{j\ge1}$ be a complete real orthonormal basis of $\mathcal{H}_0$, with $V_m = \mathrm{span}\{e_1, \dots, e_m\}$ and orthogonal projection P_m. Define

$$(\mathbf{T}_m)_{ij} = \langle T_0 e_j, e_i\rangle, \qquad \alpha_m = \lambda_{\min}(\mathbf{T}_m), \quad \beta_m = \lambda_{\max}(\mathbf{T}_m). \tag{24}$$

For $f = \sum_j c_j e_j$, $\|f\|^2 = \boldsymbol{c}^\mathsf{T}\boldsymbol{c}$ and $Q[f] = \boldsymbol{c}^\mathsf{T}\mathbf{T}_m\boldsymbol{c}$. Thus, the ordinary matrix Hessian, when these are bounded phase modes, is $2\mathbf{T}_m$.

Standard Rayleigh–Ritz and density principles give the endpoint convergence below. Interior spectral approximation for multiplication operators requires separate analysis; see Morrison [16].

Theorem 5 (Galerkin endpoint convergence)**.** *The matrix endpoints are the exact extrema of Q on the unit sphere of V_m, and*

$$\alpha_m \downarrow \alpha, \qquad \beta_m \uparrow \beta. \tag{25}$$

Proof. The finite extrema and monotonicity follow from Rayleigh–Ritz and $V_m \subset V_{m+1}$. For any unit f, the normalized projections $g_m = P_m f / \|P_m f\|$ are defined for all sufficiently large m and converge to f. Boundedness of T_0 gives $Q[g_m] \to Q[f]$. The inequalities $\alpha \le \alpha_m \le Q[g_m] \le \beta_m \le \beta$, followed by the infimum or supremum over unit f, prove both limits. □

The density argument gives convergence of endpoint values. Rates and convergence of extremal vectors require additional analysis, as discussed in Section 11.

Proposition 2 (Projection and normalization). *Let $f \in \mathcal{H}_0$ be unit, $p = P_m f$, $r = \|p\|$, and $\delta = \|f - p\|$. Then, $r^2 + \delta^2 = 1$, and for any $L \ge \|T_0\|$,*

$$|Q[f] - Q[p]| \le L\delta(1 + r), \tag{26}$$

$$r^2\alpha_m - L\delta(1 + r) \le Q[f] \le r^2\beta_m + L\delta(1 + r). \tag{27}$$

If $r > 0$, the normalized projection $\chi = p/r$ satisfies

$$\alpha_m \le Q[\chi] \le \beta_m, \qquad |Q[f] - Q[\chi]| \le 2L\sqrt{2(1 - r)}. \tag{28}$$

Proof. Orthogonality gives the norm identity. Symmetry yields $Q[f] - Q[p] = \mathcal{B}_\Omega(f - p, f + p)$, which proves (26); the finite Rayleigh bounds give (27). Finally, $\|f - \chi\|^2 = \delta^2 + (1-r)^2 = 2(1 - r)$ and $\|f + \chi\| \le 2$ prove (28). □

The normalized projection is undefined for $r = 0$. In numerical work, the residual is integrated directly instead of being computed by subtracting r^2 from one.

6. Radial Circular-Pupil Specialization

Let D be the unit disk and Ω the centered disk of dimensionless radius $q_0 \ge 0$. The radial subspace of the full disk space is identified isometrically with

$$\mathcal{H}_\mathrm{r} = L^2((0, 1), \mu; \mathbb{R}), \qquad \mathrm{d}\mu(\rho) = 2\rho\,\mathrm{d}\rho, \qquad \mathcal{H}_{\mathrm{r},0} = 1^\perp. \tag{29}$$

We write T_{q_0} for the radial phase operator and $T_{q_0,0}$ for its restriction to $\mathcal{H}_{\mathrm{r},0}$.

An optical interpretation is monochromatic scalar diffraction in the focal plane of an ideal paraxial lens. For pupil radius a_p, focal length F, wavelength λ_opt and receiver radius R_rec, the focal-plane Fourier kernel [7] (Equation (2)) gives the dimensionless scaling $q_0 = a_\mathrm{p} R_\mathrm{rec}/(\lambda_\mathrm{opt} F)$. The phase is measured in radians, so $|\epsilon|$ is its RMS for a mean-zero unit-RMS direction.

Hankel Form and Multiplication Term

Angular integration gives, for an integrable radial aperture function f,

$$U_f(q) = 2\pi \int_0^1 f(\rho) J_0(2\pi q\rho)\rho\,\mathrm{d}\rho = \pi \int_0^1 f(\rho) J_0(2\pi q\rho)\,\mathrm{d}\mu(\rho). \tag{30}$$

For $f = e^{\mathrm{i}\epsilon\psi}$, the energy is $E_{q_0}(\epsilon\psi) = 2\int_0^{q_0} |U_f(q)|^2 q\,\mathrm{d}q$. With $U^{(j)} = U_{\psi^j}$, $j = 0, 1, 2$, the quadratic coefficient and baseline are

$$Q_{q_0}[\psi] = 2\int_0^{q_0} [(U^{(1)}(q))^2 - U^{(0)}(q)U^{(2)}(q)]q\,\mathrm{d}q, \tag{31}$$

$$U^{(0)}(q) = \frac{J_1(2\pi q)}{q}, \quad U^{(0)}(0) = \pi, \qquad E_{q_0}(0) = 1 - J_0(2\pi q_0)^2 - J_1(2\pi q_0)^2. \tag{32}$$

The baseline energy follows by integrating $(J_0(t)^2 + J_1(t)^2)' = -2J_1(t)^2/t$. The spatial disk kernel is $\kappa_{q_0}(\boldsymbol{x}) = q_0 J_1(2\pi q_0|\boldsymbol{x}|)/|\boldsymbol{x}|$ for $\boldsymbol{x} \ne 0$, with $\kappa_{q_0}(0) = \pi q_0^2$.

The radial concentration kernel and multiplier are

$$k_{q_0}(\rho,s) = 2\pi^2 \int_0^{q_0} J_0(2\pi q\rho) J_0(2\pi qs) q \, \mathrm{d}q, \quad (K_{q_0} f)(\rho) = \int_0^1 k_{q_0}(\rho,s) f(s) \, \mathrm{d}\mu(s), \tag{33}$$

$$b_{q_0}(\rho) = (K_{q_0} 1)(\rho) = 2\pi \int_0^{q_0} J_0(2\pi q\rho) J_1(2\pi q) \, \mathrm{d}q, \quad T_{q_0} = K_{q_0} - M_{b_{q_0}}. \tag{34}$$

These factors follow directly from (30) and $\int_0^1 J_0(2\pi qs) \, \mathrm{d}\mu(s) = J_1(2\pi q)/(\pi q)$. In particular,

$$b_{q_0}(0) = 1 - J_0(2\pi q_0), \qquad b_{q_0}(1) = \frac{1 - J_0(2\pi q_0)^2}{2}, \qquad \left\| T_{q_0} \right\| \le \min\{\pi^2 q_0^2, 1 + \left\| b_{q_0} \right\|_\infty\}. \tag{35}$$

The kernel k_{q_0} is continuous and real symmetric, and K_{q_0} is compact, nonnegative and bounded above by the identity.

Lemma 1 (Strict positivity of radial concentration)**.** *If $q_0 > 0$ and $0 \neq f \in \mathcal{H}_\mathrm{r}$, then $\left\langle K_{q_0} f, f \right\rangle > 0$. In particular, K_{q_0} is injective.*

Proof. Suppose $\left\langle K_{q_0} f, f \right\rangle = 2 \int_0^{q_0} |U_f(q)|^2 q \, \mathrm{d}q = 0$. Nonnegativity of the integrand and continuity of U_f imply $U_f(q) = 0$ throughout $(0, q_0)$. Since μ is a probability measure, $f \in L^2(\mu)$ belongs to $L^1(\mu)$. The Bessel power series and its derivatives converge uniformly for $0 \le \rho \le 1$ and z in any compact subset of $\mathbb{C}$. Consequently, $U_f(z) = \pi \int_0^1 f(\rho) J_0(2\pi z\rho) \, \mathrm{d}\mu(\rho)$ is entire, by termwise integration. The identity theorem gives $U_f \equiv 0$. This is the two-dimensional Fourier transform of the zero-extended radial disk function at every real frequency. Fourier uniqueness, or Plancherel, then gives $f = 0$, which is a contradiction. □

Strict positivity does not imply a uniform positive lower bound: K_{q_0} is compact on an infinite-dimensional space.

7. Essential Spectrum and Finite-Dimensional Uniform Bounds

7.1. Essential Interval and an Unattained Endpoint

The general multiplication-plus-compact principle is classical [15] (Corollary 1.5). We use the essential spectrum of a bounded self-adjoint operator, equivalently the spectrum after deleting isolated eigenvalues of finite multiplicity. The singular Weyl criterion characterizes it by unit approximate eigenvectors converging weakly to zero [18] (Lemmas 6.17–6.18).

Theorem 6 (Essential interval and exact lower endpoint)**.** *For $q_0 > 0$,*

$$\sigma_{\mathrm{ess}}(T_{q_0,0}) = \left[-\max_{0 \le \rho \le 1} b_{q_0}(\rho), -\min_{0 \le \rho \le 1} b_{q_0}(\rho) \right], \tag{36}$$

$$\inf \sigma(T_{q_0,0}) = -\max_{0 \le \rho \le 1} b_{q_0}(\rho). \tag{37}$$

The operator $T_{q_0,0}$ is not compact. Its lower endpoint is not an eigenvalue and is not attained by a unit phase.

Proof. Write $b = b_{q_0}$. Multiplication by $-b$ has essential spectrum $\operatorname{ess\,ran}(-b)$. To verify this assertion, outside the essential range, the multiplier $(-b - \lambda)^{-1}$ is bounded. Inside it, each set $\{|-b - \lambda| < 1/n\}$ has positive measure. Since μ is non-atomic, choose a unit function supported there and orthogonal to the preceding finitely many choices. The resulting orthonormal sequence is weakly null and has residual at most $1/n$. The singular Weyl criterion proves the assertion. Continuity of b and full support of μ make its essential range its image, so this spectrum is the interval in (36).

A compact operator sends a bounded weakly null sequence to a norm-null sequence. Otherwise, compactness gives a subsequence with a nonzero norm limit, contradicting the weak limit zero. Therefore, adding the compact K_{q_0} preserves singular Weyl sequences in both directions, proving (36) first on $\mathcal{H}_{\mathrm{r}}$. The decomposition $\mathcal{H}_{\mathrm{r}} = \operatorname{span}\{1\} \oplus \mathcal{H}_{\mathrm{r},0}$ reduces T_{q_0}. Removing the constant component from a singular Weyl sequence changes it by a norm-null sequence; normalization gives one in $\mathcal{H}_{\mathrm{r},0}$. Conversely, a singular sequence in $\mathcal{H}_{\mathrm{r},0}$ is one in $\mathcal{H}_{\mathrm{r}}$. Thus, the same essential spectrum holds after removing the piston.

For a unit $f \in \mathcal{H}_{\mathrm{r},0}$, Lemma 1 gives

$$Q_{q_0}[f] + \max b_{q_0} = \left\langle K_{q_0} f, f \right\rangle + \int_0^1 (\max b_{q_0} - b_{q_0}) |f|^2 \, \mathrm{d}\mu > 0. \tag{38}$$

The endpoint $-\max b_{q_0}$ is already in the essential spectrum, so this proves both (37) and nonattainment. Finally, $b_{q_0}(0) > 0$: the angular cosine representation of $J_0(t)$ gives $J_0(t) < 1$ for $t > 0$. Hence, the essential spectrum contains a nonzero point, which a compact self-adjoint operator cannot have. □

At $q_0 = 0$, $K_{q_0} = b_{q_0} = T_{q_0} = 0$, and every unit phase attains both endpoints.

For fixed $q_0 > 0$, unit Galerkin minimizers $f_m \in V_m$ satisfy $Q_{q_0}[f_m] = \alpha_m \downarrow -\max b_{q_0}$ by Theorem 5. They have no strongly convergent subsequence in L^2: any such limit would remain unit and, by continuity of Q_{q_0}, attain the excluded endpoint. Thus, in quadratic phase optimization, increasing the modal resolution can improve the objective value without producing a limiting RMS-normalized optimal phase; the stability of the computed phase profiles must be assessed separately.

7.2. A Criterion for an Upper Isolated Spectral Value

Proposition 3 (Upper spectral separation)**.** *Let A be a bounded self-adjoint operator with nonempty essential spectrum, and put $\gamma = \sup \sigma_{\mathrm{ess}}(A)$. If a nonzero f satisfies*

$$\frac{\langle Af, f \rangle}{\|f\|^2} > \gamma, \tag{39}$$

then $\sup \sigma(A) > \gamma$ is an isolated eigenvalue of finite multiplicity. In particular, a radial piston-free phase satisfying $Q_{q_0}[f]/\|f\|^2 > -\min b_{q_0}$ proves such an eigenvalue for $T_{q_0,0}$.

Proof. The bounded self-adjoint spectral theorem bounds every Rayleigh quotient by $\beta = \sup \sigma(A)$ [18]. Compactness of the spectrum gives $\beta \in \sigma(A)$, and (39) gives $\beta > \gamma$. Thus, β lies outside the essential spectrum and is, by its stated definition, an isolated eigenvalue of finite multiplicity. The radial case uses the essential upper edge $-\min b_{q_0}$. □

This classical spectral criterion requires a strict inequality between the trial quotient and the essential upper edge. The rational bounds below establish that inequality independently of the floating-point spectra.

Corollary 1 (Two certified receiver radii)**.** *For each $q_0 \in \{11/10, 2\}$, the radial piston-free operator $T_{q_0,0}$ has an isolated eigenvalue of finite multiplicity strictly above its essential spectrum.*

Proof. The phase $f(\rho) = \sqrt{3}(2\rho^2 - 1)$ has zero mean and unit RMS. Exact rational integration of truncated Bessel series, with analytic tail and between-node bounds, as detailed in Appendix A, gives the strict rational inequalities

q_0	$\min b_{q_0}$	$Q_{q_0}[f]$
11/10	> 0.4088	> -0.090433
2	> 0.3333	> -0.014616

Thus, $Q_{q_0}[f] + \min b_{q_0} > 0.31$ in both cases. Proposition 3 proves the assertion. □

The common gap lower bound 0.31 extends the separation to radius intervals through (52). These certificates establish existence above the essential spectrum; the sign, precise location and number of isolated eigenvalues remain undetermined.

Corollary 2 (Finite-codimension phase constraints)**.** *Let $q_0 > 0$, and let W be a closed subspace of finite codimension in $\mathcal{H}_{r,0}$. If P_W is the orthogonal projection in $\mathcal{H}_{r,0}$, the self-adjoint compression $T_W = P_W T_{q_0,0}|_W$ has the essential spectrum in (36). Moreover,* $\inf \sigma(T_W) = -\max b_{q_0}$*, and no unit vector of W attains this value.*

Proof. Write $T_0 = T_{q_0,0}$, $P = P_W$ and $F = I - P$. The projection F has finite rank. The extension of T_W by zero on $W^\perp$ is PT_0P, and $T_0 - PT_0P = FT_0 + PT_0F$ has finite rank: the first term has finite-dimensional range, and the second factors through the range of F. Compact-perturbation invariance and deletion of the finite-dimensional zero summand preserve the essential spectrum. For unit $f \in W$, $\langle T_W f, f\rangle = \langle T_0 f, f\rangle$, so (38) still holds. The essential lower endpoint supplies the infimum, while strictness excludes attainment. □

A constrained space need not reduce T_{q_0}, so this result uses compression. Excluding finitely many low-order modes can change finite-dimensional Ritz extrema without changing the infinite-dimensional lower endpoint.

7.3. Complete Polynomial Spaces and an Exact Embedding Constant

Let P_j be the Legendre polynomial with $P_j(1) = 1$, and define

$$Z_j(\rho) = \sqrt{2j+1}\, P_j(2\rho^2 - 1), \qquad V_m = \operatorname{span}\{Z_1, \dots, Z_m\}, \qquad m \geq 1. \tag{40}$$

These are the azimuthally constant radial Zernike modes, with polynomial degree $2j$ [20]; j is not a Noll index. The substitution $x = 2\rho^2 - 1$ takes $\mathrm{d}\mu$ to $\mathrm{d}x/2$, proving orthonormality. Polynomials are dense in continuous functions on $[-1, 1]$, and continuous functions are dense in L^2 there. Thus, $Z_0 = 1, Z_1, \dots$ are complete in $\mathcal{H}_r$, and $(Z_j)_{j\geq 1}$ are complete in $\mathcal{H}_{r,0}$. Theorem 5 applies, with the lower target now given explicitly by (37).

Proposition 4 (Exact polynomial embedding)**.** *For $V_m = \operatorname{span}\{Z_1, \dots, Z_m\}$, where $Z_j(\rho) = \sqrt{2j+1} P_j(2\rho^2 - 1)$ and $m \geq 1$,*

$$C_m := \sup_{\substack{f \in V_m \\ \|f\|_2 = 1}} \|f\|_\infty = \sup_{0 \leq \rho \leq 1} \left(\sum_{j=1}^{m} Z_j(\rho)^2 \right)^{1/2} = \sqrt{m(m+2)}. \tag{41}$$

Proof. The substitution $x = 2\rho^2 - 1$ converts $2\rho\, \mathrm{d}\rho$ to $\mathrm{d}x/2$, so the modes are orthonormal and have zero mean. Pointwise Cauchy–Schwarz and the classical Legendre bound $|P_j(x)| \leq 1$ on $[-1, 1]$ [21] (Equation 18.14.1) give $|\sum c_j Z_j(\rho)|^2 \leq \sum_{j=1}^{m} (2j+1) = m(m+2)$ for $\sum c_j^2 = 1$. Equality holds at $\rho = 1$ for $c_j = \sqrt{2j+1}/\sqrt{m(m+2)}$. Continuity and positive measure of every endpoint neighborhood identify this maximum with the essential supremum. □

Corollary 3 (Finite-dimensional quartic control)**.** *For every unit $f \in V_m$ and real ϵ,*

$$\left| E_{q_0}(\epsilon f) - E_{q_0}(0) - \epsilon^2 Q_{q_0}[f] \right| \leq B_m(q_0) |\epsilon|^4, \qquad B_m(q_0) = \frac{\pi^2 q_0^2}{12} \{m(m+2) + 3\}. \tag{42}$$

Proof. $\|f\|_4^4 \leq \|f\|_\infty^2 \|f\|_2^2 \leq C_m^2$. Apply Theorem 4 and Proposition 4. □

Kernel-dependent bounds and the fourth-order coefficient. The exact embedding constant C_m yields a sufficient coefficient $B_m(q_0)$ after a fourth-moment estimate and a uniform kernel bound. To retain the kernel information, define for real radial $f \in L^4$

$$\mathcal{C}_{q_0}(f) = \frac{1}{24}\iint |k_{q_0}(\rho,s)|\,|f(\rho)-f(s)|^4\,\mathrm{d}\mu(\rho)\,\mathrm{d}\mu(s),$$
$$\mathcal{A}_{q_0}(f) = \frac{1}{24}\iint k_{q_0}(\rho,s)\,[f(\rho)-f(s)]^4\,\mathrm{d}\mu(\rho)\,\mathrm{d}\mu(s). \tag{43}$$

Writing $R_{q_0}(\epsilon f) = E_{q_0}(\epsilon f) - E_{q_0}(0) - \epsilon^2 Q_{q_0}[f]$, the cosine remainder gives $|R_{q_0}(\epsilon f)| \le \mathcal{C}_{q_0}(f)|\epsilon|^4$ for every real ϵ. Dominated convergence gives $R_{q_0}(\epsilon f)/\epsilon^4 \to \mathcal{A}_{q_0}(f)$ as $\epsilon \to 0$, with majorant $|k_{q_0}|\,|f(\rho)-f(s)|^4/24$. For mean-zero f, the bound $|k_{q_0}| \le \pi^2 q_0^2$ and the fourth-moment identity yield

$$\mathcal{C}_{q_0}(f) \le \frac{\pi^2 q_0^2}{12}\left(\|f\|_4^4 + 3\|f\|_2^4\right).$$

Thus, $\mathcal{C}_{q_0}$ gives an all-amplitude absolute bound, while $\mathcal{A}_{q_0}$ includes signed cancellation in the small-amplitude limit. The absolute value in $\mathcal{C}_{q_0}$ is essential: the kernel can change sign even though K_{q_0} is a positive operator.

For V_1, the unit directions are $\pm Z_1$ and $\|Z_1\|_4^4 = 9/5$. Hence,

$$|R_{q_0}(\epsilon Z_1)| \le \frac{2\pi^2 q_0^2}{5}|\epsilon|^4, \qquad \frac{2\pi^2 q_0^2}{5} < B_1(q_0) = \frac{\pi^2 q_0^2}{2} \quad (q_0 > 0). \tag{44}$$

The one-mode fourth moment therefore lowers the sufficient coefficient by 20%; the optimal coefficient remains open. The nonlinear-extrema bounds below retain the general B_m for all m.

For $W_m = \mathrm{span}\{Z_3, \ldots, Z_m\}$ with $m \ge 3$, the same argument gives the exact squared embedding constant $m(m+2) - 8$. The direct supremum estimate in (7) instead gives the larger coefficient $2\pi^2 q_0^2 m^2 (m+2)^2/3$.

Corollary 4 (Finite nonlinear extrema)**.** *Let $F_m^-(\epsilon)$ and $F_m^+(\epsilon)$ be the minimum and maximum of $E_{q_0}(\epsilon f)$ over unit $f \in V_m$. They exist, and*

$$|F_m^-(\epsilon) - E_{q_0}(0) - \epsilon^2\alpha_m| \le B_m(q_0)\epsilon^4, \qquad |F_m^+(\epsilon) - E_{q_0}(0) - \epsilon^2\beta_m| \le B_m(q_0)\epsilon^4. \tag{45}$$

If an extremal matrix eigenvalue has a positive gap g to the next distinct eigenvalue, each corresponding nonlinear optimizer f_ϵ, for $\epsilon \ne 0$, satisfies

$$\mathrm{dist}(f_\epsilon, \mathcal{E}_m)^2 \le \frac{2B_m(q_0)\epsilon^2}{g}, \tag{46}$$

where $\mathcal{E}_m$ is that extremal eigenspace.

Proof. The finite sphere is compact, and the energy is continuous in its coefficients. Apply (42) to every unit phase and then to a unit extremal eigenvector to obtain (45). Comparing a nonlinear minimizer with such an eigenvector bounds its Rayleigh excess by $2B_m(q_0)\epsilon^2$. Orthogonal eigenspace decomposition bounds this excess below by $g\,\mathrm{dist}(f_\epsilon, \mathcal{E}_m)^2$. The maximum case is analogous. If the matrix has only one distinct eigenvalue, the distance to its full eigenspace is zero. □

In (46), the distance is to the eigenspace of the fixed finite matrix, rather than to its unit sphere.

8. Obstruction to Uniform L^2 Quadratic Expansion

The full L^2 unit sphere contains arbitrarily high phases on shrinking supports. In the sequence below, a fixed nonzero phase difference occupies a set of vanishing measure, so the RMS tends to zero. The normalized direction changes with the support, preventing the uniform approximation that holds on L^4-bounded classes.

Proposition 5 (Radial obstruction to second-order Fréchet expansion)**.** *For the unit disk and $q_0 > 0$, let $\mathcal{H}_{\mathrm{r},0} = \{f \in L^2((0,1), 2\rho\,\mathrm{d}\rho; \mathbb{R}) : \int f\, 2\rho\,\mathrm{d}\rho = 0\}$. There is no bounded symmetric bilinear form $\mathfrak{H}$ on this space such that*

$$E_{q_0}(h) = E_{q_0}(0) + \tfrac{1}{2}\mathfrak{H}(h,h) + o(\|h\|_2^2) \quad \text{as } h \to 0 \text{ in } \mathcal{H}_{\mathrm{r},0}. \tag{47}$$

There are also no constants $C < \infty$, $\epsilon_0 > 0$ giving $|E_{q_0}(\epsilon f) - E_{q_0}(0) - \epsilon^2 Q_{q_0}[f]| \le C|\epsilon|^4$ for every bounded unit $f \in \mathcal{H}_{\mathrm{r},0}$ and $|\epsilon| \le \epsilon_0$.

Proof. Use the continuous radial concentration kernel k_{q_0} and multiplier $b_{q_0} = K_{q_0}1$. Their normalization gives $E_{q_0}(h) = \iint k_{q_0} \cos(\Delta h)\,\mathrm{d}\mu\,\mathrm{d}\mu$, without an additional area factor. Moreover $b_{q_0}(0) = 1 - J_0(2\pi q_0) > 0$; the angular cosine representation of $J_0(t)$ makes it strictly less than one for $t > 0$.

Fix $a \neq 0$ and, for $0 < \delta \le 1/2$, let $B_\delta = \{\rho \in (0,1) : \rho < \sqrt{\delta}\}$. The support radius is $\sqrt{\delta}$, whereas its probability measure is $\mu(B_\delta) = \int_0^{\sqrt{\delta}} 2\rho\,\mathrm{d}\rho = \delta$. Set $h_\delta = a(\mathbf{1}_{B_\delta} - \delta)$. Then,

$$\int h_\delta\,\mathrm{d}\mu = a\{\delta - \delta\} = 0,$$
$$\|h_\delta\|_2^2 = a^2\{\delta(1-\delta)^2 + (1-\delta)\delta^2\} = a^2\delta(1-\delta).$$

Define

$$D_\delta = \int_{B_\delta} b_{q_0}\,\mathrm{d}\mu - \iint_{B_\delta \times B_\delta} k_{q_0}\,\mathrm{d}\mu\,\mathrm{d}\mu.$$

Continuity of b_{q_0} and boundedness of k_{q_0} give $D_\delta/\delta \to b_{q_0}(0)$: the second integral is $O(\delta^2)$. The phase difference is zero within each region and $\pm a$ between regions, so

$$E_{q_0}(h_\delta) - E_{q_0}(0) = 2(\cos a - 1)D_\delta, \qquad Q_{q_0}[h_\delta] = -a^2 D_\delta. \tag{48}$$

Since $\|h_\delta\|_2^2 = a^2\delta(1-\delta) \to 0$,

$$\frac{E_{q_0}(h_\delta) - E_{q_0}(0) - Q_{q_0}[h_\delta]}{\|h_\delta\|_2^2} \longrightarrow \frac{a^2 + 2(\cos a - 1)}{a^2} b_{q_0}(0) > 0. \tag{49}$$

Strict positivity follows from $1 - \cos a < a^2/2$ for $a \neq 0$. If (47) held, the fixed-direction expansion in Proposition 1 would force $\mathfrak{H}(f,f) = 2Q_{q_0}[f]$; polarization then identifies its entire bilinear form with $2\langle T_{q_0} f, g\rangle$. Equation (49) contradicts the required remainder.

Finally, write $h_\delta = \epsilon_\delta f_\delta$ with $\epsilon_\delta = a\sqrt{\delta(1-\delta)}$ and $f_\delta = (\mathbf{1}_{B_\delta} - \delta)/\sqrt{\delta(1-\delta)}$. Each f_δ is bounded, mean-zero and unit, while $\epsilon_\delta \to 0$. The absolute remainder divided by $|\epsilon_\delta|^4$ equals $[a^2 + 2(\cos a - 1)]|D_\delta|/[a^4\delta^2(1-\delta)^2]$ and diverges. □

The directions f_δ vary with δ, so $h_\delta = \epsilon_\delta f_\delta$ does not approach zero along a fixed ray. The fixed-direction second Gâteaux derivative controls ϵf for each fixed f, whereas a second-order Fréchet expansion must control all L^2 perturbations approaching zero. The positive limit in (49) shows that the normalized remainder does not vanish along this varying-direction sequence.

Corollary 5 (Obstruction on the full two-dimensional phase space)**.** *For $q_0 > 0$, both nonexistence conclusions in Proposition 5 hold on the full piston-free space $L^2_0(D, \mathrm{d}\boldsymbol{r}/\pi; \mathbb{R})$ of the unit disk and, hence, also on its full real L^2 phase space.*

Proof. The radial inclusion $Jf(\boldsymbol{r}) = f(|\boldsymbol{r}|)$ is an isometry because polar integration gives $\|Jf\|^2_{L^2(D,\mathrm{d}\boldsymbol{r}/\pi)} = \int_0^1 |f(\rho)|^2\, 2\rho\, \mathrm{d}\rho$. It preserves the mean and has closed range. Angular integration identifies the restricted full-disk energy and quadratic coefficient with their radial forms. A full-space second-order Taylor expansion would restrict under J to one on the radial piston-free space, with a bounded restricted bilinear form and the same little-o property. A full-space uniform quartic bound would also restrict to the radial unit sphere. Both contradict Proposition 5. The final assertion follows by restricting the full L^2 space to its piston-free subspace. □

Full Fourier energy and other kernels. The obstruction concerns energy captured by a finite receiver. For the full Fourier plane, Plancherel's identity gives

$$E_{\mathbb{R}^2}(h) = \frac{1}{S}\int_{\mathbb{R}^2} |\widehat{Ae^{ih}}(\boldsymbol{q})|^2\, \mathrm{d}\boldsymbol{q} = \frac{1}{S}\int_D A^2\, \mathrm{d}\boldsymbol{r} = 1 \tag{50}$$

for every real measurable phase. This constant functional has vanishing variations of every order. The full-plane identity follows directly from Plancherel, whereas the bounded-kernel representation used above assumes a finite-measure receiver.

For other cosine-difference functionals on the same radial probability space, let k be a real bounded continuous symmetric kernel, and set $b_k(\rho) = \int k(\rho, s)\, \mathrm{d}\mu(s)$. The concentrating-set calculation applies to shrinking sets A_δ satisfying $\mu(A_\delta) = \delta$ and $\delta^{-1}\int_{A_\delta} b_k\, \mathrm{d}\mu \to b_k(\rho_*) \neq 0$. Indeed, the cross-set integral equals $\int_{A_\delta} b_k\, \mathrm{d}\mu - \iint_{A_\delta \times A_\delta} k\, \mathrm{d}\mu\, \mathrm{d}\mu$, whose second term is $O(\delta^2)$ by boundedness of k. Its nonzero first-order term in δ gives the same remainder obstruction. The argument requires a nonzero multiplier limit and the cosine remainder; other cases need a separate analysis.

9. Dependence on Receiver Radius

The radial operator also varies continuously with receiver radius. This estimate extends the certificates in Corollary 1 and separates spectral variation from cumulative-energy monotonicity.

Proposition 6 (Operator-norm continuity)**.** *For receiver radii $r_1, r_2 \geq 0$,*

$$\left\|T_{r_2} - T_{r_1}\right\| \leq \pi^2 |r_2^2 - r_1^2|. \tag{51}$$

The infinite-dimensional Rayleigh endpoints and every fixed Galerkin endpoint obey the same modulus of continuity.

Proof. The two frequency disks are nested, so $\left\|\kappa_{r_2} - \kappa_{r_1}\right\|_\infty \leq \pi |r_2^2 - r_1^2|$. Apply the product-space argument of (14) to the difference of the two forms, with $S = \pi$, to obtain (51). A unit Rayleigh quotient changes by at most this norm. Taking infima or suprema, either over the full sphere or a fixed finite sphere, proves the endpoint assertion. □

On $[0, R]$, the bound is Lipschitz with constant $2\pi^2 R$. The multiplier satisfies $\left\|b_{r_2} - b_{r_1}\right\|_\infty \leq \pi^2 |r_2^2 - r_1^2|$, so the essential endpoints are continuous as well.

Persistence of the certified upper separation. Keep the unit trial phase $f = \sqrt{3}(2\rho^2 - 1)$ fixed, and put $g(q) = Q_q[f] + \min b_q$. The Rayleigh and multiplier bounds imply

$$|g(q) - g(q_*)| \leq 2\pi^2 |q^2 - q_*^2|. \tag{52}$$

At either $q_* \in \{11/10, 2\}$, Corollary 1 gives $g(q_*) > 31/100$. Thus, $g(q) > 0$ whenever $|q^2 - q_*^2| \leq 31/(200\pi^2)$. In particular, the following closed intervals are certified:

$$q \in [219/200, 221/200] = [1.095, 1.105], \qquad q \in [1997/1000, 2003/1000] = [1.997, 2.003]. \tag{53}$$

Indeed, the largest squared-radius differences are 441/40,000 and 12,009/1,000,000, respectively, and $\pi < 22/7$ makes each loss in (52) strictly less than 31/100. Proposition 3 then gives an isolated eigenvalue above the essential spectrum throughout both intervals. These certified intervals are sufficient neighborhoods; determining their maximal extent remains open.

Proposition 7 (Cumulative energy and its difference from the baseline)**.** *For a bounded real radial phase ϕ, the exact cumulative energy is nondecreasing in the receiving radius. For $q_0 > 0$,*

$$\frac{\mathrm{d}}{\mathrm{d}q_0} E_{q_0}(\phi) = 2q_0 |U_{e^{\mathrm{i}\phi}}(q_0)|^2 \geq 0. \tag{54}$$

If $e^{\mathrm{i}\phi}$ is not constant almost everywhere, then $\Delta(q_0) = E_{q_0}(\phi) - E_{q_0}(0)$ is not monotone on $[0, \infty)$.

Proof. The Hankel field is continuous, so differentiation of its energy integral gives (54) for $q_0 > 0$; at zero, the right derivative is zero. The strict triangle inequality, with its equality condition, gives $|U_{e^{\mathrm{i}\phi}}(0)| = \pi |\int_0^1 e^{\mathrm{i}\phi}\,\mathrm{d}\mu| < \pi = U^{(0)}(0)$ when $e^{\mathrm{i}\phi}$ is not almost everywhere constant. Continuity then makes the perturbed intensity strictly smaller than the baseline intensity for all sufficiently small frequencies. Integrating their difference with weight $2q$ yields $\Delta(q_0) < 0$ for all sufficiently small $q_0 > 0$, whereas $\Delta(0) = 0$. Plancherel gives $E_{q_0}(\phi) \to 1$ and $E_{q_0}(0) \to 1$ as $q_0 \to \infty$, so $\Delta(q_0) \to 0$. These facts exclude both nondecreasing and nonincreasing behavior on the full half-line. □

For example, $\phi(\rho) = \epsilon\rho^2$ satisfies the nonconstant-field condition for every $\epsilon \neq 0$. Nonmonotonicity here concerns the energy difference and does not require a change in its sign.

10. Numerical Examples

10.1. Model and Quadrature

The computations use the uniform unit disk with probability measure $2\rho\,\mathrm{d}\rho$, receiver radii $q_0 = 0.5, 1.1, 2$, and dimensions $m = 4, 8, 12, 16, 24, 32, 48, 64$. The reported values from (31) use Gauss–Legendre quadrature with 768 radial and 512 frequency nodes. Refinement comparisons use $(256, 192)$, $(512, 384)$ and $(1536, 768)$ radial/frequency pairs. The finest pair provides the reference for matrices, multipliers and selected nonlinear energies.

For each configured matrix through $m = 64$, we compare the Hankel assembly with $K_{q_0} - M_{b_{q_0}}$ and angular integration of the spatial difference kernel. Direct integration of the complex Fourier field uses 160 radial, 120 frequency and 256 angular nodes. A separate difference-kernel calculation of Q uses 160 radial and 512 angular nodes. These calculations differ from the Hankel results by at most 1.854×10^{-14} for energy and 4.274×10^{-14} for Q.

The largest scaled eigenpair residual is 1.326×10^{-15}. The residual $\|\mathbf{T}_m v - \lambda v\|_2$ is divided by $\max\{1, \|\mathbf{T}_m\|_2\}$, with v of unit norm and the induced Euclidean matrix norm. Separate radial, frequency and basis refinements also check normalization and matrix symmetry.

Five prescribed mean-zero, unit-RMS profiles are Z_1, Z_4, $(Z_1 + Z_2)/\sqrt{2}$, and the two radial cosine profiles

$$\psi_k(\rho) = \frac{\cos(2\pi k\rho) - \mu_k}{s_k}, \qquad \mu_k = \int_0^1 \cos(2\pi k\rho)\,\mathrm{d}\mu, \qquad s_k^2 = \int_0^1 (\cos(2\pi k\rho) - \mu_k)^2\,\mathrm{d}\mu, \tag{55}$$

with $k = 0.75$ and 6. Here, k is the dimensionless oscillation parameter of the prescribed radial profile. Amplitude halving from $\epsilon = 0.4$ to 0.00625 probes the remainder scaling. Further calculations use finite Ritz vectors and the bound (42).

Role and reproducibility of the computations. The scans and energy curves describe the computed finite-dimensional responses. Quadrature refinement, alternative integration formulas and matrix residuals check their numerical accuracy. The infinite-dimensional separation follows from Appendix A and Section 9; the topology obstruction follows from (48).

The data and code archive provides the numerical outputs, configurations and figure-generation scripts. It also includes exact-rational and directed-rounding interval implementations of the spectral certificates, with derivations and execution instructions.

10.2. Projection and Modal Content

The equal-RMS cosine profiles have different modal distributions (Figure 1). The larger-k profile ψ_6 retains a substantial projection residual in V_{16}, whereas its residual in V_{32} is approximately 1.905×10^{-11}. Residuals were integrated directly, avoiding subtraction of nearly equal squared norms. Table 1 compares each original profile with its normalized finite projection. The latter lies in the finite spectral interval; the former is covered by the projection correction in (27).

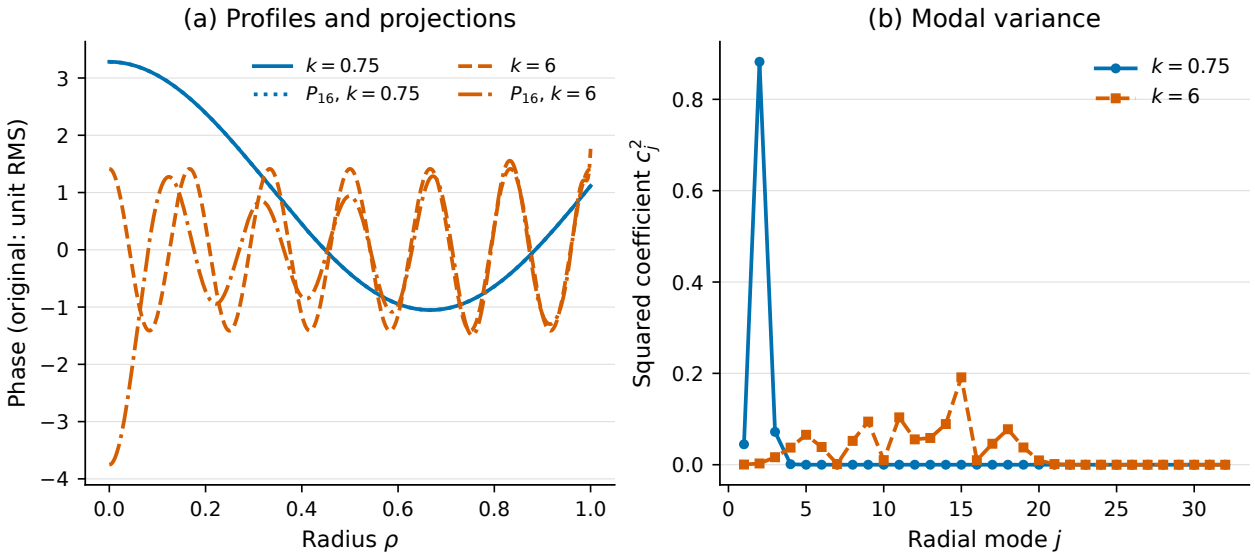

Figure 1. Unit-RMS cosine profiles and their unrenormalized 16-mode projections (**a**); squared modal coefficients through $j = 32$ (**b**). For $k = 0.75$, the dotted projection curve is indistinguishable from the solid original curve at the plotting scale.

Table 1. Projection quantities at $q_0 = 1.1$: $r^2 = \|P_m\psi_k\|_2^2$, $\delta = \|\psi_k - P_m\psi_k\|_2$, and $\chi_m = P_m\psi_k/r$. The residual is directly integrated.

k	m	r^2	δ	$Q[\psi_k]$	$Q[\chi_m]$
0.75	4	0.999995	2.305×10^{-3}	−0.182096	−0.182462
0.75	16	1.000000	7.563×10^{-13}	−0.182096	−0.182096
6	4	0.057018	9.711×10^{-1}	−0.908986	−0.655506
6	16	0.827458	4.154×10^{-1}	−0.908986	−0.861966
6	32	1.000000	1.905×10^{-11}	−0.908986	−0.908986

10.3. Receiver Radius and Finite Extrema

The radius scan uses 119 equally spaced radii from 0.05 to 3, with $m = 4, 8, 16, 32, 64$ and $(512, 384)$ quadrature nodes. Figure 2 shows how the nested finite spectral intervals vary with receiver radius.

Table 2 compares finite endpoints with numerical estimates of $-\max b_{q_0}$. At $q_0 = 1.1$, the upper endpoint changes little beyond $m = 16$, while the lower endpoint continues to decrease. The limiting lower value has no unit minimizer by Theorem 6.

Table 2. Finite Ritz endpoints and numerical estimates of $-\max b_{q_0}$. The last column is estimated by grid sampling and local optimization.

q_0	m	α_m	β_m	$-\max b_{q_0}$ (Numerical)
0.5	4	−1.182718	−0.487405	
0.5	16	−1.294991	−0.456720	
0.5	64	−1.303678	−0.453927	−1.304242
1.1	4	−0.938287	0.116236	
1.1	16	−1.136260	0.119487	
1.1	64	−1.160470	0.119487	−1.162188
2	4	−0.589292	0.039032	
2	16	−1.069070	0.054702	
2	64	−1.103140	0.054702	−1.105662

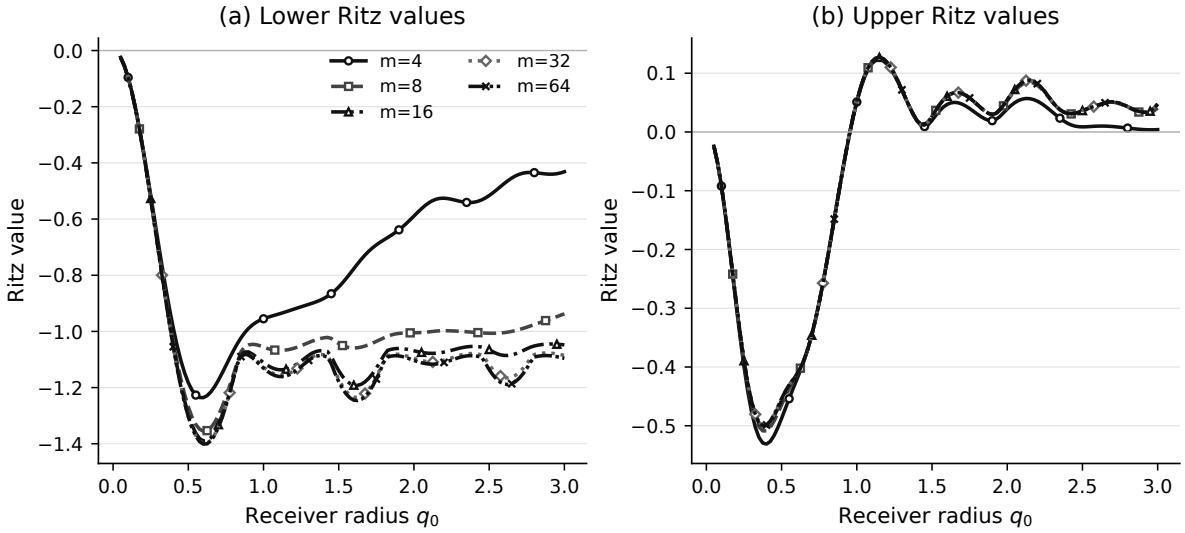

Figure 2. Lower (**a**) and upper (**b**) Ritz endpoints versus receiver radius. Lines connect the 119 computed radius samples; line styles and markers identify five nested polynomial dimensions. The same line styles and markers are used in both panels. The endpoint convergence is given by Theorem 5.

Excluding selected modes can also change the sign of the largest finite response. At $q_0 = 1.1$, the computed maximum is 0.119486636 in V_{16} and −0.466081946 in W_{16}, which excludes Z_1 and Z_2. Removing finitely many modes leaves the infinite-dimensional lower endpoint unchanged by Corollary 2.

10.4. Nonlinear Energy and Quartic Control

Figure 3 compares the nonlinear energy, evaluated by quadrature, with its quadratic approximation along the maximizing V_{16} direction at $q_0 = 1.1$. The deterministic envelope $B_{16}(q_0)\epsilon^4$ from Corollary 3 applies uniformly to all unit phases in that space. Across 252 finite Ritz-vector cases, the largest computed remainder-to-bound ratio is 0.2511. Figures S1 and S2 provide the corresponding curves at $q_0 = 0.5$ and 2.

For the five prescribed profiles, the final amplitude-halving ratios give quartic orders between 3.99938 and 4.00072. Table 3 shows the increasing uniform coefficient as the

admissible finite dimension grows. The L^4 calculation also applies beyond bounded phases. A further numerical example uses

$$f(\rho) = \frac{\sqrt{147}}{2}\left(\rho^{-1/4} - \frac{8}{7}\right), \qquad f \in L^4 \setminus L^\infty, \qquad \int f \, d\mu = 0, \quad \|f\|_2 = 1.$$

Its nonlinear remainder, evaluated with transformed quadrature near the origin, remains below the bound in Theorem 4 at the sampled amplitudes. This example illustrates why a fourth-moment condition is less restrictive than a supremum bound.

Table 3. Embedding constants C_m rounded to six decimals and sufficient quartic coefficients. The B_m column uses the L^4 bound in Corollary 3; the last column gives the L^∞-based coefficient divided by $\pi^2 q_0^2$.

m	$C_m = \sqrt{m(m+2)}$	$B_m/(\pi^2 q_0^2)$	L^∞-Based Coarse Coefficient$/(\pi^2 q_0^2)$
4	4.898979	2.250000	384.000000
16	16.970563	24.250000	55,296.000000
32	32.984845	90.916667	789,162.666667
64	64.992307	352.250000	11,894,784.000000

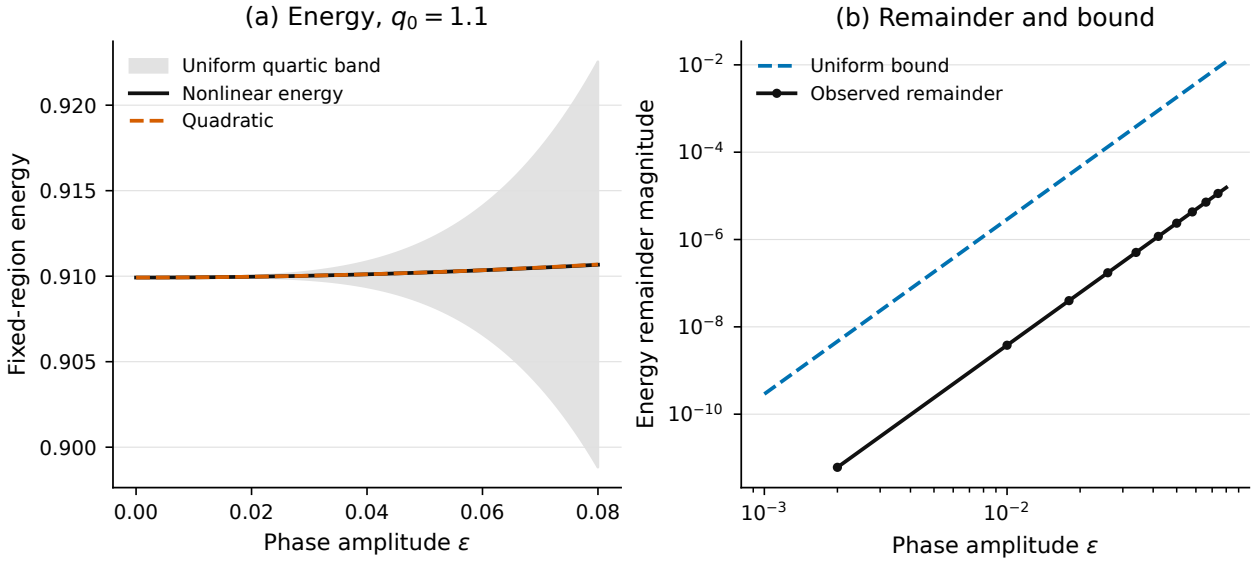

Figure 3. Nonlinear energy evaluated by quadrature and its quadratic approximation along the maximizing direction in V_{16} at $q_0 = 1.1$ (**a**); absolute remainder and uniform quartic bound (**b**). The shaded band has half-width $B_{16}(q_0)\epsilon^4$ about the quadratic prediction. Values at or below 10^{-12} are omitted from the logarithmic curve and retained in the data. Figures S1 and S2 show the other two radii.

10.5. Basis Refinement and the Essential Interval

Figure 4 separates changes under basis refinement from the quadrature differences in Table 4. Table 4 also reports the absolute eigenpair residual. At the largest displayed dimension, the lower-endpoint gaps remain larger than the quadrature changes, whereas the upper values stabilize more rapidly. Theorem 5 identifies the limits; the plotted increments quantify changes between successive modal dimensions.

Table 4. Maximum observed agreement metrics. Refinement compares lower-node rules with the highest-node reference. These floating-point differences and residuals are not rigorous error enclosures.

Comparison	Maximum Observed Value
Matrix entries under quadrature refinement	1.001×10^{-11}
All eigenvalues under quadrature refinement	2.346×10^{-10}
Nonlinear energy under quadrature refinement	2.925×10^{-13}
Quadratic coefficient under quadrature refinement	2.147×10^{-10}
Multiplier on the radial grid under refinement	2.408×10^{-13}
Hankel energy versus direct angular integration	1.854×10^{-14}
Hankel quadratic coefficient versus spatial kernel	4.274×10^{-14}
Spike energy: split quadrature versus support identity	2.076×10^{-14}
Finite eigenpair residual (Euclidean norm)	1.460×10^{-15}

The multiplier extrema are estimated on a 2001-point radial grid, followed by local optimization and comparison with the boundary values. Figure 5 compares the resulting essential-interval estimate with the finite Ritz spectra at $q_0 = 1.1$. Figures S3 and S4 show the other two radii. The rigorous separation results are given in Corollary 1 and extended to radius intervals in Section 9.

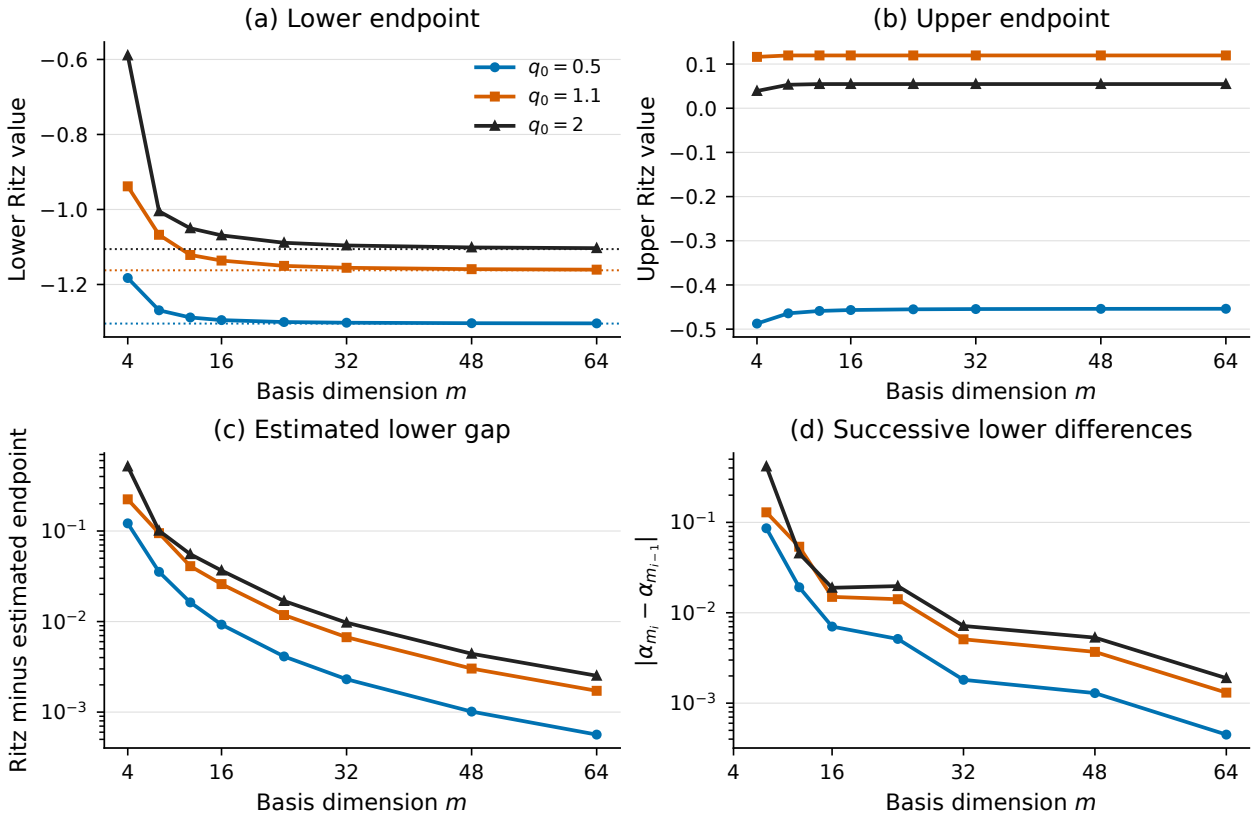

Figure 4. Lower (**a**) and upper (**b**) Ritz endpoints and the remaining lower gap (**c**). In panel (**a**), horizontal dotted lines show numerical estimates of $-\max b_{q_0}$, with colors matching the corresponding q_0 curves. Panel (**d**) plots $|\alpha_{m_i} - \alpha_{m_{i-1}}|$ at m_i for consecutive dimensions $4, 8, 12, 16, 24, 32, 48, 64$. These are successive finite-dimensional increments, not errors relative to the limiting endpoint. No convergence rate is fitted.

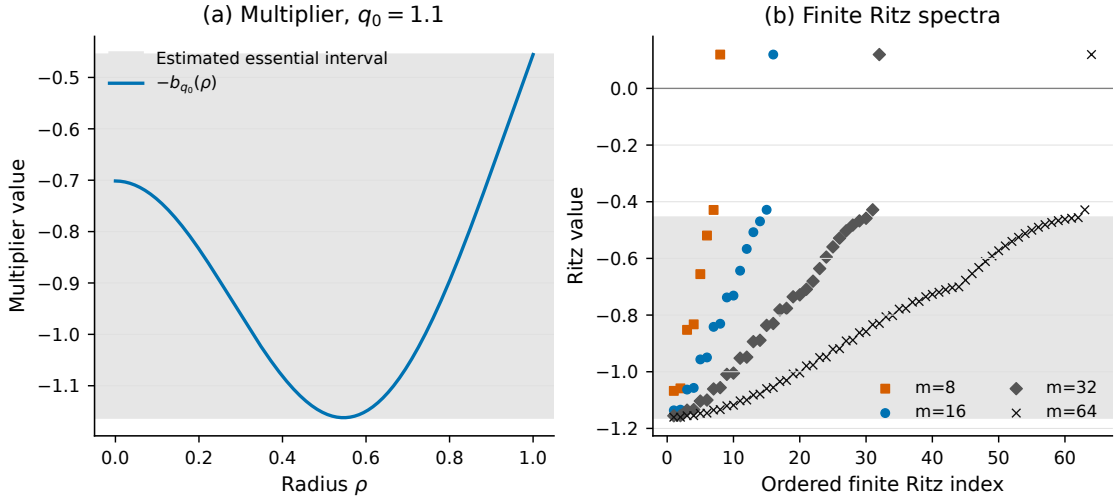

Figure 5. Numerical multiplier (**a**) and finite Ritz spectra (**b**) at $q_0 = 1.1$. The shaded essential interval uses estimated multiplier extrema. Corollary 1 gives the rigorous separation certificate. Figures S3 and S4 show $q_0 = 0.5, 2$.

10.6. Concentrating Phases

The sequence in Proposition 5 uses $a = 1$ and $\delta = 2^{-j}, j = 4, \ldots, 18$. Splitting quadrature at $\rho = \sqrt{\delta}$ resolves the concentrating region, with 128 nodes on each side and 512 frequency nodes. The support transform has the independent expression $U_{\mathbf{1}_{B_\delta}}(q) = \sqrt{\delta} J_1(2\pi q\sqrt{\delta})/q$, with continuous value $\pi\delta$ at zero. It evaluates the exact remainder identity in (48) without subtracting nearly equal energies. Direct split-support integration supplies the energy comparison in Table 4.

In Figure 6, the normalized remainder approaches the positive limit in (49), while the unit-RMS peak grows. Across the three radii, the final three normalized remainders differ from their limits by approximately 0.0634% or less. These curves illustrate the nonuniformity of the fixed-direction quadratic expansion over the RMS unit sphere.

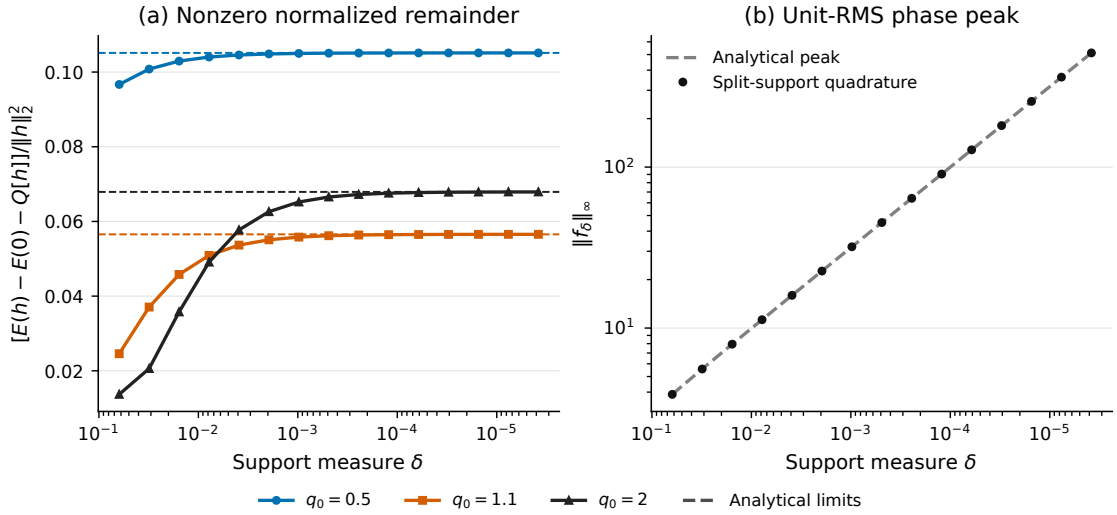

Figure 6. Concentrating phases and the L^2 topology obstruction. The remainder divided by $\|h_\delta\|_2^2$ approaches a positive limit (**a**), while the unit-RMS phase peak increases (**b**). In panel (**a**), horizontal dashed lines show the analytical limits for the corresponding receiver radii, using the same colors as the numerical curves. In panel (**b**), the gray dashed line shows the analytical unit-RMS phase peak. The concentrating set has probability-area measure δ and radius $\sqrt{\delta}$; the mean-zero phase includes a constant background outside this set.

11. Discussion

For phase-only perturbations, the baseline-field cross term changes the spectral optimization problem. The resulting multiplication term places it in the multiplication-plus-compact setting studied by Biberdorf and Väth and Morrison [15,16]. Although finite modal spaces have optimizing phases, their lower endpoints approach a value that no unit phase attains. Thus, convergence of extremal values does not imply strong convergence of the corresponding minimizing phases.

The admissible phase class also determines the reliability of nonlinear predictions. A common L^4 bound controls the remainder even when pointwise phase values are unbounded. On V_m, the coefficient B_m provides this control from an RMS constraint, but its growth with m gives no dimension-independent estimate. The stronger impossibility statement follows from Proposition 5, which rules out any uniform quartic bound on the full unit sphere.

The same concentration mechanism explains the differentiability hierarchy in Table 5. Fixed-direction differentiation remains valid. For concentrating perturbations, however, the remainder divided by the squared RMS approaches a nonzero limit. This connects the nonlocal energy functional with concentration effects in superposition operators on Lebesgue spaces [19]. The full-plane energy is constant, so this regularity limitation depends on restricting the receiving region.

Table 5. Differentiability of the fixed-region energy. The first four rows assume uniform amplitude and a finite centrally symmetric receiver (Proposition 1). The last row concerns the unit disk with a centered receiver of positive radius (Proposition 5 and Corollary 5).

Property	Scope	Holds
First Fréchet derivative	Entire real phase space	Yes
Globally Lipschitz first derivative	Entire real phase space	Yes
Fixed-direction second Gâteaux derivative	At zero; convergence in $\mathcal{H}^*$	Yes
Finite-dimensional Hessian	At zero; bounded phase modes	Yes
Full-L^2 second-order Fréchet Taylor expansion	At zero; full or piston-free disk space	No

The radial spectral conclusions apply to a uniform circular aperture in the dimensionless coherent scalar propagation model. Classifying upper separation outside (53) would determine how far the certified spectral behavior extends in receiver radius. Convergence rates for Ritz approximations to isolated upper eigenspaces also remain to be quantified. For nonlinear bounds, the one-mode improvement in (44) motivates optimization of the kernel-dependent coefficient beyond the sufficient estimate B_m.

12. Conclusions

The compact-minus-multiplication representation links fixed-region phase variation to spectral bounds and finite modal approximations. For radial phases on a disk with uniform aperture amplitude and a centered disk receiver, it gives an exact essential-spectrum characterization, an unattained lower endpoint and certified upper separation on two radius intervals; these spectral conclusions have not been extended here to general apertures or nonuniform amplitudes. Uniform quartic remainder estimates justify nonlinear approximation on L^4-bounded phase classes, including every fixed polynomial modal sphere. On the full RMS sphere, concentrating phases rule out both uniform quartic control and a second-order Fréchet Taylor expansion at zero. Spectral approximation and nonlinear remainder control therefore require separate checks when the admissible phase space is

enlarged. Within the uniform radial disk model, these bounds provide a mathematical basis for assessing the fixed-region energy response of finite modal wavefront descriptions.

Supplementary Materials: The following supporting information can be downloaded at https://www.mdpi.com/article/10.3390/math14214093/s1, Supplementary Information: Figures S1–S4 are provided in the accompanying file supplementary_information.pdf. Figure S1: Energy and quartic control at $q_0 = 0.5$. (a) Nonlinear energy evaluated by quadrature and its quadratic approximation along the maximizing direction in V_{16}. The shaded band has half-width $B_{16}(q_0)\epsilon^4$. (b) Absolute remainder and uniform quartic bound. Values at or below 10^{-12} are retained in the CSV and are omitted from the logarithmic curve. Figure S2: Energy and quartic control at $q_0 = 2$. (a) Nonlinear energy and its quadratic approximation along the maximizing direction in V_{16}, with the uniform quartic band. (b) Absolute remainder and uniform bound. The quadrature evaluation, amplitude grid and logarithmic display convention are the same as in Figure S1. Figure S3: Multiplier and finite Ritz spectra at $q_0 = 0.5$. (a) The negative multiplier $-b_{q_0}(\rho)$ and estimated essential interval. (b) Ritz values in the four polynomial spaces. Figure S4: Multiplier and finite Ritz spectra at $q_0 = 2$. (a) The negative multiplier and the estimated essential interval. (b) Ritz values, including values above the displayed interval. The certificate establishes upper spectral separation at this radius; the locations and number of plotted outliers remain numerical estimates.

Author Contributions: Conceptualization, Y.H.; Formal analysis, L.Z.; Funding acquisition, Y.H.; Investigation, N.Z.; Methodology, Y.H., R.L. and L.Z.; Software, R.L.; Supervision, L.Z.; Validation, H.J. and N.Z.; Visualization, N.Z.; Writing—original draft, H.J.; Writing—review & editing, Y.H. All authors have read and agreed to the published version of the manuscript.

Funding: This research was supported by the National Natural Science Foundation of China, Grant No. 62405245.

Institutional Review Board Statement: Not applicable.

Informed Consent Statement: Not applicable.

Data Availability Statement: The raw data supporting the conclusions of this article will be made available by the authors on request.

Conflicts of Interest: The authors declare no conflict of interest.

Appendix A. Exact Rational Certificate for Two Upper Spectral Values

Fix the trial phase $f(\rho) = \sqrt{3}(2\rho^2 - 1)$ used in Corollary 1, and set $T = 2\pi q_0$. Termwise integration of the J_0 series gives

$$U_f(q) = -\sqrt{3}J_3(2\pi q)/q, \qquad U_{f^2}(q) = [J_1(2\pi q) + 2J_5(2\pi q)]/q.$$

Indeed, the moments of $f/\sqrt{3}$ and f^2 against ρ^{2j} are, respectively, $j/[(j+1)(j+2)]$ and $3(j^2+j+2)/[(j+1)(j+2)(j+3)]$. Therefore,

$$Q_{q_0}[f] = 2\int_0^T \frac{3J_3(t)^2 - J_1(t)^2 - 2J_1(t)J_5(t)}{t}\,\mathrm{d}t, \qquad b_{q_0}(\rho) = \int_0^T J_0(t\rho)J_1(t)\mathrm{d}t. \tag{A1}$$

The certificate encloses π by the Machin identity

$$\pi = 16\arctan(1/5) - 4\arctan(1/239).$$

We use the first 32 terms and the next term of each alternating series. Integer outward rounding to 40 decimal places gives rational bounds and, hence, $T_{\mathrm{lo}} \le T \le T_{\mathrm{hi}}$. Put $T_* = (T_{\mathrm{lo}} + T_{\mathrm{hi}})/2$ and $dT = (T_{\mathrm{hi}} - T_{\mathrm{lo}})/2$. For $M = 32$ and $n \in \{0, 1, 3, 5\}$, define

$$P_n(t) = \sum_{j=0}^{M} \frac{(-1)^j (t/2)^{2j+n}}{j!(j+n)!}, \quad p_n = 2(M+1) + n, \quad r_n = \frac{T_*^2}{4(M+2)(M+n+2)},$$

$$E_n = \frac{(T_*/2)^{p_n}}{(M+1)!(M+1+n)!(1-r_n)}.$$

The inequality $r_n < 1$ and the successive omitted-term ratios in the Bessel series give $|J_n(t) - P_n(t)| \le E_n(t/T_*)^{p_n}$ on $[0, T_*]$. The integer-order integral representation gives $|J_n(x)| \le 1$ for real x [21] (Equations 10.2.2 and 10.9.2).

Let $b_P(\rho) = \int_0^{T_*} P_0(t\rho)P_1(t)\,\mathrm{d}t$. Splitting the product error gives

$$e_b = T_*\left\{\frac{E_0}{p_0+1} + \frac{(1+E_0)E_1}{p_1+1}\right\}.$$

Since $J_0' = -J_1$, $|b_{q_0}'(\rho)| \le T_{\mathrm{hi}}^2/2$. Every point in $[0,1]$ is within $1/(2N)$ of one of the $N+1$ mesh points i/N, with $N = 256$. Thus,

$$\min b_{q_0} \ge \min_{0\le i\le N} b_P(i/N) - e_b - dT - \frac{T_{\mathrm{hi}}^2}{4N}. \tag{A2}$$

This bounds the entire interval, including the points between mesh nodes.

Let Q_P denote (A1) with J_n replaced by P_n and upper endpoint T_*. The square and product error estimates give

$$e_Q = 2\left[\frac{3E_3(2+E_3)}{p_3} + \frac{E_1(2+E_1)}{p_1} + 2\left\{\frac{E_1}{p_1} + \frac{(1+E_1)E_5}{p_5}\right\}\right] + \frac{12dT}{T_{\mathrm{lo}}},$$

and $Q_P - e_Q \le Q_{q_0}[f] \le Q_P + e_Q$. The endpoint term follows from the exact integrand bound $12/t$; the series terms are integrable at zero because $p_n > 0$. Every polynomial integral, mesh evaluation, and error bound is computed with exact rational arithmetic. The exact-rational certificate script evaluates the weaker rational bounds used in Corollary 1. An independent calculation encloses the same trial quotients and multiplier minima by outward-rounded interval evaluation of a spatial-kernel series and a Bernstein polynomial bound.

Table A1 displays the resulting rational enclosures. The upper bound for the multiplier minimum follows by evaluating at a mesh point minimizing b_P, giving $\min b_{q_0} \le \min_i b_P(i/N) + e_b + dT$.

Table A1. Certified intervals for the unit trial $f(\rho) = \sqrt{3}(2\rho^2 - 1)$, from the exact-rational calculation with $M = 32$ and $N = 256$. Endpoints are rounded outward to six decimal places. The last column adds the displayed lower endpoints, proving $Q_{q_0}[f] > -\min b_{q_0}$.

q_0	$Q_{q_0}[f]$	$\min_{\rho\in[0,1]} b_{q_0}(\rho)$	Lower Bound for $Q_{q_0}[f] + \min b_{q_0}$
11/10	$[-0.090433, -0.090432]$	$[0.408804, 0.455454]$	$0.318371 > 0.31$
2	$[-0.014616, -0.014615]$	$[0.333383, 0.487596]$	$0.318767 > 0.31$

References

1. Slepian, D.; Pollak, H.O. Prolate Spheroidal Wave Functions, Fourier Analysis and Uncertainty—I. *Bell Syst. Tech. J.* **1961**, *40*, 43–63. [CrossRef]
2. Slepian, D. Prolate Spheroidal Wave Functions, Fourier Analysis and Uncertainty—IV: Extensions to Many Dimensions; Generalized Prolate Spheroidal Functions. *Bell Syst. Tech. J.* **1964**, *43*, 3009–3057. [CrossRef]
3. Clements, A.M.; Wilkins, J.E., Jr. Apodization for Maximum Encircled-Energy Ratio and Specified Rayleigh Limit. *J. Opt. Soc. Am.* **1974**, *64*, 23–27. [CrossRef]
4. Mazilu, M.; Baumgartl, J.; Kosmeier, S.; Dholakia, K. Optical Eigenmodes; Exploiting the Quadratic Nature of the Energy Flux and of Scattering Interactions. *Opt. Express* **2011**, *19*, 933–945. [CrossRef] [PubMed]
5. Sivaramakrishnan, A.; Lloyd, J.P.; Hodge, P.E.; Macintosh, B.A. Speckle Decorrelation and Dynamic Range in Speckle Noise–Limited Imaging. *Astrophys. J.* **2002**, *581*, L59–L62. [CrossRef]
6. Perrin, M.D.; Sivaramakrishnan, A.; Makidon, R.B.; Oppenheimer, B.R.; Graham, J.R. The Structure of High Strehl Ratio Point-Spread Functions. *Astrophys. J.* **2003**, *596*, 702–712. [CrossRef]

7. Antonello, J.; Verhaegen, M.; Fraanje, R.; van Werkhoven, T.; Gerritsen, H.C.; Keller, C.U. Semidefinite Programming for Model-Based Sensorless Adaptive Optics. *J. Opt. Soc. Am. A* **2012**, *29*, 2428–2438. [CrossRef] [PubMed]
8. Aryan, H.; Boreman, G.D.; Suleski, T.J. Simple Methods for Estimating the Performance and Specification of Optical Components with Anisotropic Mid-Spatial Frequency Surface Errors. *Opt. Express* **2019**, *27*, 32709–32721. [CrossRef] [PubMed]
9. Aryan, H.; Boreman, G.D.; Suleski, T.J. The Minimum Modulation Curve as a Tool for Specifying Optical Performance: Application to Surfaces with Mid-Spatial Frequency Errors. *Opt. Express* **2019**, *27*, 25551–25559. [CrossRef] [PubMed]
10. Hefferan, T.; Graves, L.; Trumper, I.; Pak, S.; Kim, D. Parametric Mid-Spatial Frequency Surface Error Synthesis. *Photonics* **2021**, *8*, 584. [CrossRef]
11. Liu, D.; Mu, D.; Liu, H.; Zhang, T.; Yu, J.; Zhang, S.; Li, Y. Investigation on the Influence of Mid-Spatial-Frequency Surface Figure Errors on Imaging Quality of Optical Systems. *Appl. Opt.* **2026**, *65*, 8685–8698. [CrossRef]
12. DeMars, L.A.; Suleski, T.J. Pupil-Difference Moments for Estimating Relative Modulation from General Mid-Spatial Frequency Surface Errors. *Opt. Lett.* **2023**, *48*, 2492–2495. [CrossRef] [PubMed]
13. DeMars, L.A.; Suleski, T.J. Use of Pupil-Difference Moments for Predicting Optical Performance Impacts of Generalized Mid-Spatial Frequency Surface Errors. *Opt. Express* **2023**, *31*, 36337–36349. [CrossRef] [PubMed]
14. DeMars, L.A.; Bauer, A.; Stone, B.D.; Rolland, J.P.; Suleski, T.J. Workflow for Modeling of Generalized Mid-Spatial Frequency Errors in Optical Systems. *Opt. Express* **2024**, *32*, 2688–2703. [CrossRef] [PubMed]
15. Biberdorf, E.A.; Väth, M. On the Spectrum of Orthomorphisms and Barbashin Operators. *Z. Für Anal. Und Ihre Anwendungen* **1999**, *18*, 859–873. [CrossRef]
16. Morrison, K.E. Spectral Approximation of Multiplication Operators. *N. Y. J. Math.* **1995**, *1*, 75–96.
17. Boulsane, M. Non-Asymptotic Behavior and the Distribution of the Spectrum of the Finite Hankel Transform Operator. *Integral Transform. Spec. Funct.* **2021**, *32*, 948–968. [CrossRef]
18. Teschl, G. *Mathematical Methods in Quantum Mechanics: With Applications to Schrödinger Operators*, 2nd ed.; Graduate Studies in Mathematics; American Mathematical Society: Providence, RI, USA, 2014; Volume 157. [CrossRef]
19. Appell, J.; Zabrejko, P.P. The Superposition Operator in Lebesgue Spaces. In *Nonlinear Superposition Operators*; Cambridge University Press: Cambridge, UK, 1990; Chapter 3, pp. 89–118. [CrossRef]
20. Noll, R.J. Zernike Polynomials and Atmospheric Turbulence. *J. Opt. Soc. Am.* **1976**, *66*, 207–211. [CrossRef]
21. Olver, F.W.J.; Olde Daalhuis, A.B.; Lozier, D.W.; Schneider, B.I.; Boisvert, R.F.; Clark, C.W.; Miller, B.R.; Saunders, B.V.; Cohl, H.S.; McClain, M.A. (Eds.) NIST Digital Library of Mathematical Functions. Release 1.2.8 of 2026-09-15; Equations (10.2.2), (10.9.2), and (18.14.1). 2026. Available online: https://dlmf.nist.gov/ (accessed on 7 October 2026).

Disclaimer/Publisher's Note: The statements, opinions and data contained in all publications are solely those of the individual author(s) and contributor(s) and not of MDPI and/or the editor(s). MDPI and/or the editor(s) disclaim responsibility for any injury to people or property resulting from any ideas, methods, instructions or products referred to in the content.